The Dance of Death: Magnetic Cataclysmic Variables

Ravi Kumar, Sparsh Gupta, Shuban Ramesh Gupta, and Abhinna Sundar

Krittika Summer Projects 2023

The Dance of Death: Magnetic Cataclysmic Variables

Ravi Kumar[1,2], Sparsh Gupta[3], Shuban Ramesh Gupta[3], and Abhinna Sundar[*,4]

[1]Krittika - The Astronomy Club of IIT Bombay, Powai, Mumbai - 400076, India

[2]Indian Institute of Technology Bombay, Mumbai - 400076, India

[3]Indian Institute of Science Education and Research, Pune - 411008, India

[4]Max Planck Institute for Astronomy (MPIA), Heidelberg - 69117, Germany

[*]Mentor for the project

Abstract

Magnetic Cataclysmic Variables (MCVs) are semi-detached binary systems with a highly magnetic white dwarf as the primary star, accreting material from a secondary red dwarf (or late-main-sequence star). The variation in the brightness of Magnetic Cataclysmic Variables provides a direct measure for calculating orbital periods and conducting temporal analysis of these variables.

In this study, we focus on the AM Her type of MCVs, where the mass transfer from the secondary to the primary white dwarf is dominated by a high magnetic field (on the order of ~ 10 MG) of the white dwarf. Utilizing images captured by the Ultra-Violet Imaging Telescope (UVIT), one of the five payloads on ISRO's AstroSat satellite, we identify and analyze three specific MCVs: AR Uma, QS Tel, and BL Hyi.

The images used in this analysis are L1-level images obtained from the AstroSat archive and require further processing to generate the final image. To achieve this, we employ a Data Reduction Pipeline provided by the software CCDLAB, which applies necessary corrections (FPN, Flat-field, Distortion, Drift, PSF) to the L1 images. Subsequently, we plot the surface brightness profile of these systems and conclude that they are not extended sources.

We then use the L2 UVIT data from the AstroSat archive to conduct temporal analysis of the systems using Python. We plot the light curves to visualize the variation of the system's brightness over the observation period. We also plot the power spectrum to find the orbital period before folding the light curve to the orbital period to find out the accretion mode. We use the aforementioned analyses to discern various properties of the system like the flux, accretion state, and orbital period.

Contents

1. Introduction

1.1 Binary Stars

A binary star is a system of two stars that are gravitationally bound to and in orbit around each other. Binary stars in the night sky that are seen as a single object to the naked eye are often resolved using a telescope as separate stars, in which case they are called visual binaries. Many visual binaries have long orbital periods of several centuries or millennia and therefore have orbits that are uncertain or poorly known. They may also be detected by indirect techniques, such as spectroscopy (spectroscopic binaries) or astrometry (astrometric binaries).
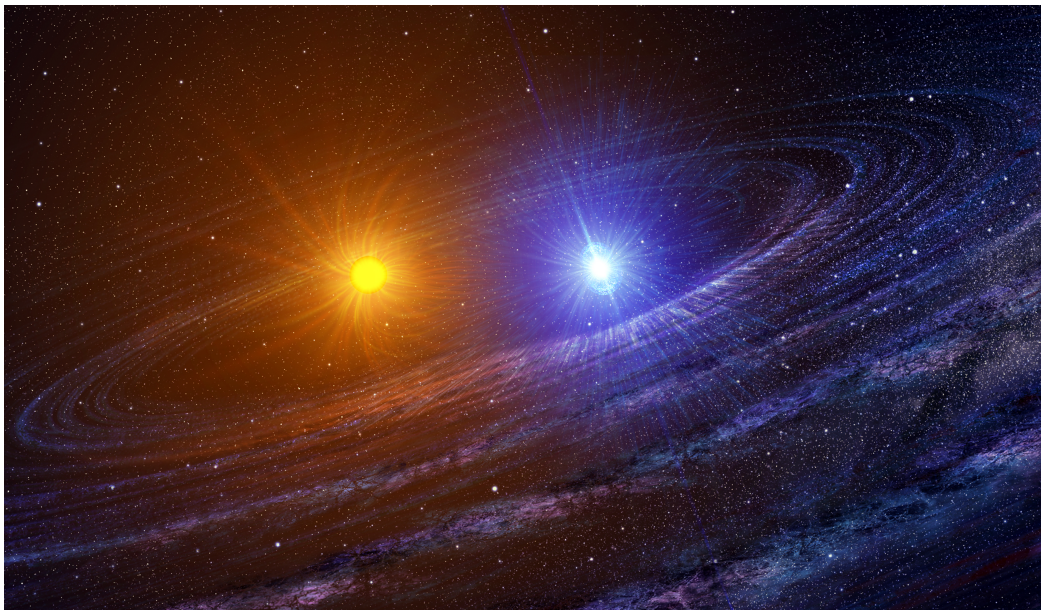

Figure 1.1: Artist depiction of the RS Ophiuchi binary system (Source: Casey Reed)

1.1.1 Types of Binaries

A **visual binary** is a binary system in which the component stars of the system can be individually resolved through a telescope. Long-term observations can then be made to plot the relative positions of the members of the system. Over time this data is accumulated and used to calculate the orbits of the stars.

If a binary star happens to orbit in a plane along our line of sight, its components will eclipse and transit each other; these pairs are called eclipsing binaries, or, together with other binaries that change brightness as they orbit, **photometric binaries**.

The majority of binary systems have been detected by Doppler shifts in their spectral lines. Such systems are called **spectroscopic binaries**. If a binary system is unresolved into its components then the spectrum obtained from it will actually be a combination of the spectra from each of the component stars. As these stars orbit each other one star, A, may be moving towards us whilst the other, B, may be moving away. The spectrum from A will therefore be blue-shifted to higher frequencies (shorter wavelengths) whilst B's spectrum will be red-shifted. If the stars are moving across our line of sight then no Doppler shifting occurs so the lines stay in their mean positions. As the stars continue orbiting, A will recede so its spectral lines will move towards the red end of the spectrum and B's will move toward the blue.

Some stars, if observed repeatedly over time, show a perturbation or "wobble" in their proper motion. If this is a periodic occurrence we can infer that the perturbation occurs due to the gravitational influence of an unseen companion. We have a system in which a visible star and a dimmer companion orbit a common centre of mass. Binary systems detected by such astrometric means are called **astrometric binaries**.

If components in binary star systems are close enough they can gravitationally distort their mutual outer stellar atmospheres. In some cases, these close binary systems can exchange mass, which may bring their evolution to stages that single stars cannot attain. Examples of binaries are Sirius, and Cygnus X-1

1.2 Cataclysmic Variables

Cataclysmic variables (CVs) are binary star systems that have a white dwarf and a normal star companion. They are typically small – the entire binary system is usually the size of the Earth-Moon system – with an orbital period of 1 to 10 hours. The white dwarf is often referred to as the "primary" star, and the normal star as the "companion" or the "secondary" star.

A white dwarf and a red dwarf spinning around each other at a very close distance lead to mass transfer from the red dwarf to the white dwarf. A white dwarf is typically much smaller, denser, and brighter than its companion red dwarf. The outer, "fluffy" layers of the red dwarf get pulled by the gravity of the white dwarf and eventually "spill" over and onto the white dwarf.
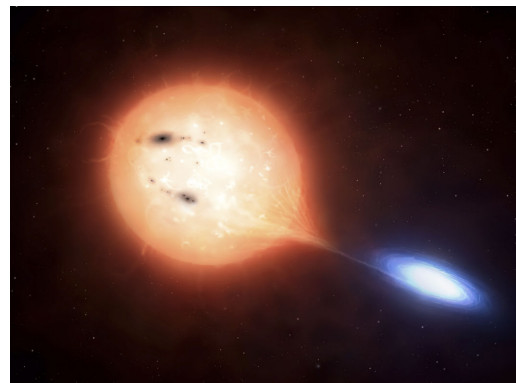

Figure 1.2: Artist depiction of a CV (Source: Mark A. Garlick)

1.2.1 Roche Lobe

The Roche lobe is the region around a star in a binary system within which orbiting material is gravitationally bound to that star. The *shape* of the Roche lobe is determined only by the mass ratio $q = M_2/M_1$ where M_2 is the mass of the red dwarf and M_1 is the mass of the white dwarf. The *scale* of the lobe is set by the size of the orbit.
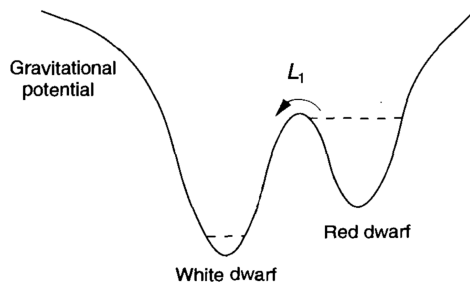
As matter fills up the Roche lobe, it eventually overflows and sinks into the Roche lobe of the white dwarf. This occurs at the inner Lagrange point. A red dwarf that fills up its Roche lobe ends up being tidally locked to the white dwarf. This happens as the "bulge" of mass requires a continuous flow of material into and out of it as the star rotates and revolves, which expends a large amount of energy, thus the star matches its spin to the orbital period.

Figure 1.3: A Schematic of Roche Lobes (Source: Coel Hellier)
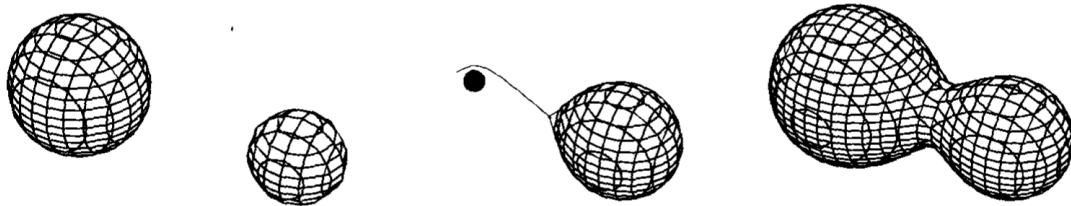
Figure 1.4: Left: A detached binary with both stars within their Roche lobes. Middle: A semi-detached binary: the secondary fills its Roche lobe emitting a stream of material from L1. If the primary is small enough, the stream will orbit around it. If it were larger, the stream would hit the primary. Right: A contact binary, with both stars overfilling their Roche lobes. (Source: Coel Hellier)

The above figure shows the different kinds of binaries based on the size of the member stars compared to their Roche Lobes. Cataclysmic Variables are of the semi-detached kind.

1.2.2 Accretion

As material flows from the secondary to the primary, the matter flows in the form of a stream or jet, and ends up in orbit around the primary, as this matter accumulates, it spreads itself into a relatively thin disc around the primary, starting from the surface of the white dwarf, to the edge being limited by tidal interactions with the secondary red dwarf.

The inner edge gets fed into the white dwarf and material is replenished by the red dwarf via the jet. This disc is known as the accretion disc, this disc is also present in black holes.

On the right, we have the accretion disc of a non-magnetic Cataclysmic Variable, seen in one plane. We can see that the accretion disc extends to the surface of the star - this is where the star starts to take in material.

The point where the stream of material from the secondary intersects the disc often releases a large amount of energy and light, thus known as the *bright spot*.
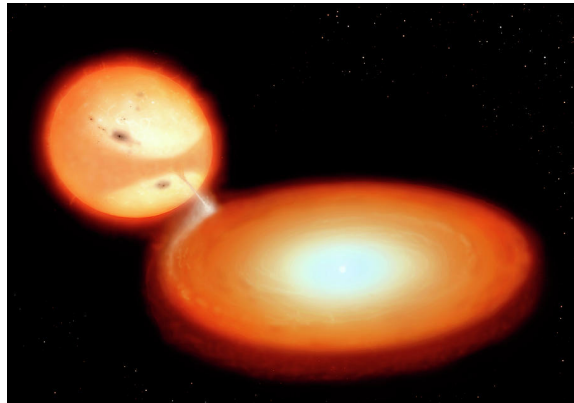

Figure 1.5: Accretion Disc of a CV (Source: Mark A. Garlick)

1.2.3   Origin of Cataclysmic Variables

The stars destined to become cataclysmic variables begin as binaries separated by a few hundred solar radii, orbiting every $\sim$10 years; one must be less than a solar mass, the other more massive. The heavier of the two stars expands and becomes a red giant, transferring its outer layers to the smaller companion star (which later becomes the white dwarf).

As the larger star loses mass, the center of mass shifts away from it and results in the decrease of stellar distance between the two stars. This decrease in the distance leads to a decrease in the Roche lobes, thus the larger star ends up filling its lobe again and drains more material. The result is a runaway feedback as the entire *envelope* of the red giant is dumped onto the companion star, limited only by the speed at which the material can flow.

The distance between the stars shrinks from about 1000 solar radii (R_o) to 1 solar radius in the span of a thousand years. This shrinkage decreases the orbital period of the stars, allowing them to rotate faster around each other, resulting in a *push-back* effect on the outer layers of the envelope mentioned earlier. The outer layers shed away from the binary and form a *planetary nebula*. The binary is finally revealed as a cataclysmic binary or, if its separation is too large, a detached red-dwarf/white-dwarf binary.

Figure 1.6: Cat's Eye Nebula - A planetary nebula formed by a binary star (Source: NASA)

1.2.4   Mass Transfer

As mass gets transferred from the secondary to the white dwarf, the center of mass shifts towards the heavier white dwarf, leading to an increase in separation between the two stars, which causes an increase in the size of the Roche lobes, halting further mass transfer.

For a steady flow of matter between the 2 stars, the angular momentum of the system should continuously decrease to compensate for the mass flow. The two main mechanisms theorized for this loss are magnetic braking and gravitational radiation.

Magnetic Braking

A star typically has a magnetic field, whose strength increases with the rotation of the star around its own axis. This rotation is very high in the case of the secondary star as it is tidally locked to the white dwarf. The particles that possess an electric charge are forced to go along the strong magnetic fields of the secondary, and thus co-rotate with it. The particles in turn take substantial angular momentum along with them, trying to slow down the rotation of the secondary about its own axis, but since it is tidally locked, this results in a decrease in orbital period instead.
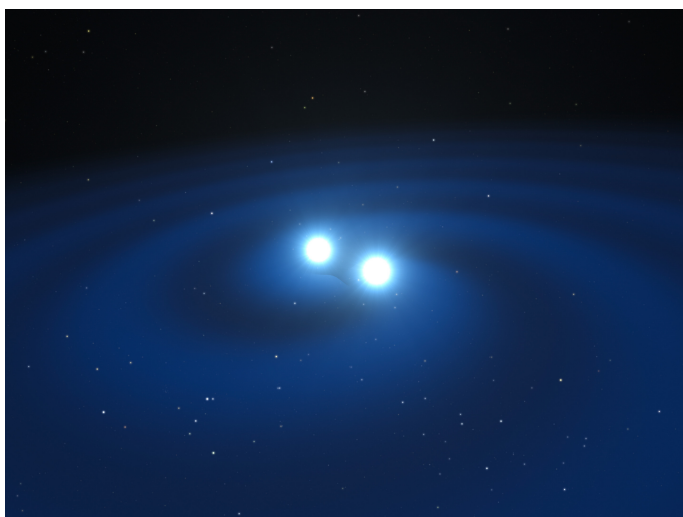
Gravitaional Radiation

Figure 1.7: Gravitational Waves caused by neutron stars (Source: ESO)

The stars move around each other with great angular velocity (typically their period of revolution is less than half a day). The repetitive orbiting of two stars causes a rhythmic warping of space which ripples outwards in a periodic wave, called gravitational radiation. This is also known as Gravitational Waves - one of the predictions of Albert Einstein's General Theory of Relativity. This effect is weaker in comparison to magnetic braking.

Neither of these theories, however, can explain the much higher (10-100 times) mass transfer rates seen in many systems.

1.2.5 Orbital Periods and the Period Gap

Longer Periods

The lower number of binaries found above an orbital period of 10 hours owes to the fact that neither the white dwarf nor red dwarf can be above the Chandrasekhar limit $\approx 1.4 M_S$. A few white dwarfs, however, are as heavy as the Chandrasekhar limit, so the $q < 1$ requirement begins to reduce the number of systems from upwards of $\sim$6 hours.

The Period Gap

The vastly lower number of binaries found with orbital periods between 2-3 hours is caused to a change in the method via mass transfer occurs. Till a period of about 3 hours, mass transfer is caused mainly due to magnetic braking, then the
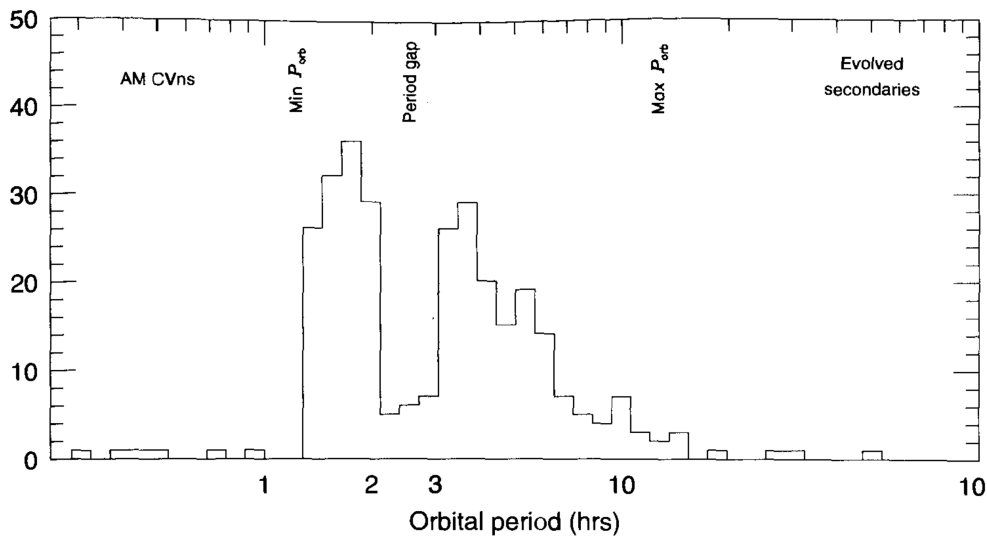
Figure 1.8: The distribution of orbital periods (Source: Coel Hellier)

gravitational radiation becomes dominant, and magnetic braking stops. The secondary was in equilibrium due to mass transfer and magnetic braking which decreased the mass to a point where the gravitational force and pressure from the core of the star are not equal in strength. Thus when the braking stops, the star shrinks in radius and does not fill up its Roche lobe anymore.

Although there is no mass transfer going on between the stars, they are losing energy due to gravitational waves, overall reducing the orbital time and separation between the stars. As the orbital time approaches 2 hours, the stars once again come back into contact, and mass transfer starts once more, but at a slower rate this time owing to the less effective gravitational radiation.

This entire process discussed above leads to a reduction in the brightness of the system when mass transfer doesn't occur. Subsequently, the system becomes too dim to be detected. The few binaries found in this orbital period range are binaries that naturally formed with a period between 2 and 3 hours.

Shorter Periods

The minimum period of systems is found to be around 78 minutes. As discussed earlier the material transfers to the white dwarf, and the secondary responds by shrinking. When the mass gets depleted to a certain amount, the secondary starts behaving like a white dwarf, i.e. it expands when it loses mass (contrary to normal stars that expand when they gain mass and contract when they lose mass). The reason for this is that normal stars are "propped" up by the pressure of gasses in their core, but a white dwarf is held together by the quantum-mechanical requirement of Pauli's exclusion principle. So, the secondary expands and thus increases the orbital period.
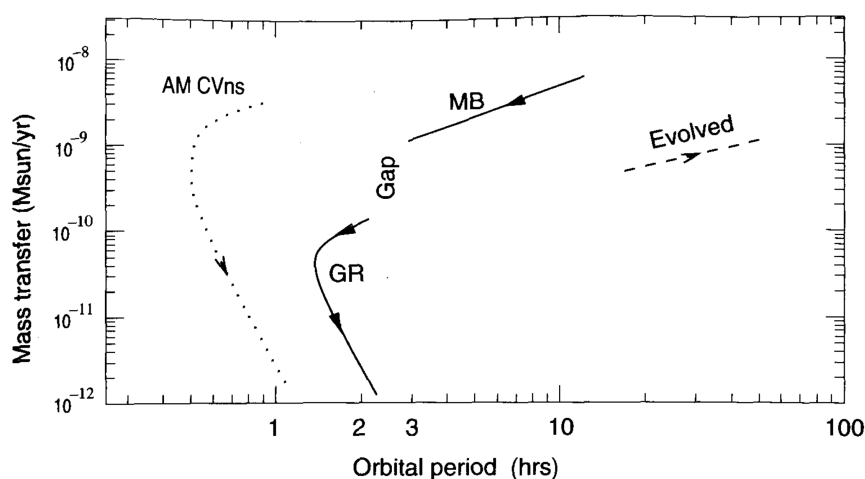
Figure 1.9: The evolution of cataclysmic variables proceeds by magnetic braking (MB) above the gap, and then by gravitational radiation (GR) below the gap and through the period minimum. The helium systems (AM CVns) evolve on a similar track at shorter periods. Systems with evolved secondaries are at longer periods. Arrows show the direction of evolution. (Source: Coel Hellier)

1.3 Magnetic Cataclysmic Variables - AM Hers

Polars, or AM Herculis stars, are a subclass of cataclysmic variables consisting of a close interacting binary system containing a white dwarf primary with a magnetic field on the order of 10–200 MG. The white dwarf is paired with a low-mass main-sequence secondary, and both stars are tidally locked with the binary period, which is generally between 80 minutes and 4 hours.

The secondary acts as a mass donor for the white dwarf, overflowing its Roche lobe and transferring mass at the inner Lagrangian point. The transferred mass, unable to form an accretion disk due to the white dwarf's high magnetic field, instead forms an accretion column that accretes over a small area covering only a few thousand square kilometers near the magnetic pole.

The interactions of the magnetic field with the stream of particles originating from the secondary interact in 2 ways that are understood fully. One is when the kinetic energy of the particles far exceeds the strength of the field, thus the field can be neglected and the particles pass straight through. The other is when the field energy is strong enough to overpower the kinetic energy of the particles, and the particles are forced to change direction and travel along the field lines.

The transition between these two regions is not fully understood as of yet. The magnetically dominated region is known as the magnetosphere and its extent is mainly determined by the strength of the field and the accretion rate.

1.3.1 Synchronous Orbits

Due to the flow of matter only along the magnetic field lines at the start of the magnetosphere, this creates a tidal locking effect, in which the material just outside the magnetosphere rotates as fast as the material just inside the sphere, thus tidally locking the white dwarf to the secondary. This mainly occurs due to the "intertwining" of the magnetic field of the white dwarf with the field of

the secondary. This "intertwining" creates a slowing down torque until the two magnetic fields stop moving with respect to each other.
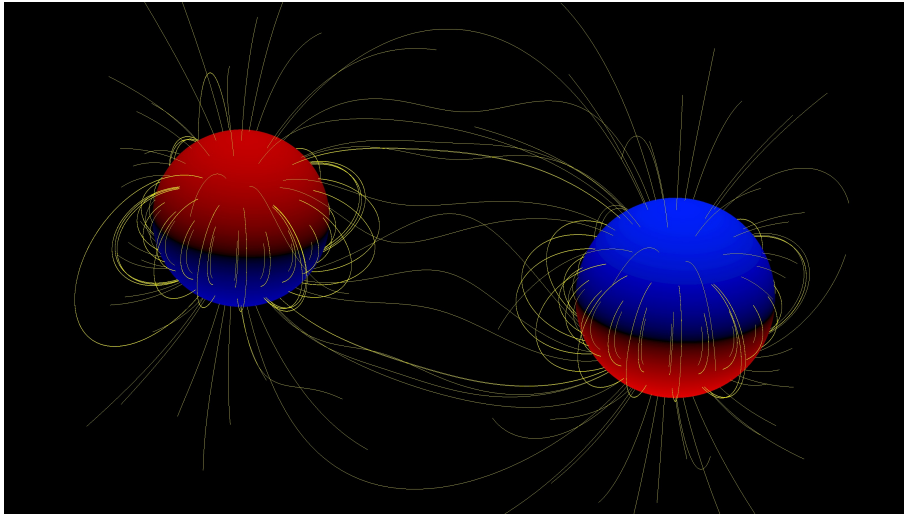

Figure 1.10: Interactions between the magnetic field of two stars
(Source: CFHT)

1.3.2 Asynchronous Orbits

As stated above, the magnetic field interactions between the 2 stars is likely the main cause for this synchronicity of orbits, but when the fields are weak enough, this torque may not be strong enough to slow down the white dwarf's spin thus leading to asynchronicity in the orbit. The material flows along multiple field lines as they pass through the point of contact of the stream with the magnetosphere.

1.3.3 Accretion Streams

AR Uma - depicted to the right has a magnetic field strength of 230MG (23000T) while a typical AM Her star has magnetic field strengths between 10 and 80MG. The material first flows along a stream, unaffected by the magnetic field, then it "hits" the magnetic field which causes it to slow down and settle at that point, known as the stagnation point. The magnetic pressure builds up at this point forcing the matter to travel along the magnetic field lines and reach the poles. There are two types of matter found here, one in the form of blobs and the other as a mist.
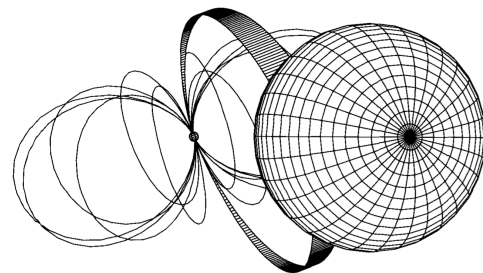

Figure 1.11: In AR Uma the accretion stream emerges from the L_1 point, splits into two, and follows the field lines onto the magnetic poles of the white dwarf (Source: Coel Hellier)

Physical systems tend to be in their lowest energy state, but for the matter to travel along the field lines, it must move out of the plane of rotation, which requires energy. To minimize this diversion, many systems are found to have the magnetic field of the white dwarf tilted over such that one of the poles faces the matter stream as shown on the left - A schematic AM Her star showing the ballistic portion of the

Figure 1.12: Accretion Stream (Source: Coel Hellier)

stream between the L1 point and the stagnation region, SR, followed by the flow onto the magnetic poles. Typically the denser, heavier "blobs" of matter flow along the shorter path, and the "mist" flows along the longer path.
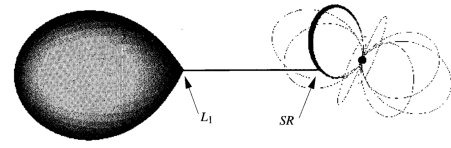
The luminosity or apparent brightness of MCVs gives a direct measure of mass-transfer rates from the Red dwarf secondary on to the primary white dwarf. Optimal modeling, allows us to determine the accretion state of the system.

1.3.4 Cyclotron Emissions

The charged particles move in circles around the magnetic field line due to the fact that the particles act like a current and the force on a current is perpendicular to the magnetic field. They also move forward along the field lines, thus creating a cyclotron motion. Since they are moving in a circle, they are constantly being accelerated, and accelerating charged particles emit photons (radiation).

This emission, for slower-moving particles, occurs at a certain frequency, known as the cyclotron frequency, For faster-moving particles, the frequency of emission is an integer multiple of the cyclotron frequency. The emission also creates "cyclotron humps" in the spectrum.

The cyclotron frequency ω_c, of an electron in a magnetic field B is eB/m_e rad s^{-1}, where e is the electron charge and m_e its mass. Thus the frequency of the emitted light is $\nu_c = eB/2\pi m_e$ Hz

Using the above equation and the frequency of the hump created, it's possible to calculate the strength of the magnetic field of the system.

1.3.5 Zeeman Splitting

Typically in an atom, the orbitals are oriented in a specific direction. This direction normally doesn't affect the energy of the orbit but in the presence of strong magnetic fields, like in the case of magnetic cataclysmic variables, the energy of the orbital depends on its orientation with the magnetic field, thus the spectral lines are shifted slightly and split into different components, known as Zeeman splitting. The degree of splitting depends on magnetic field strength and thus measuring the splitting in the spectrum data gives us the field strength.
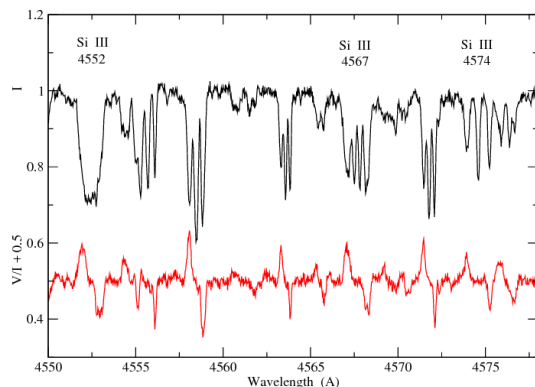

Figure 1.13: The upper spectrum shows Zeeman splitting of the strongly magnetic star HD 215441. (Source: John Darlington)
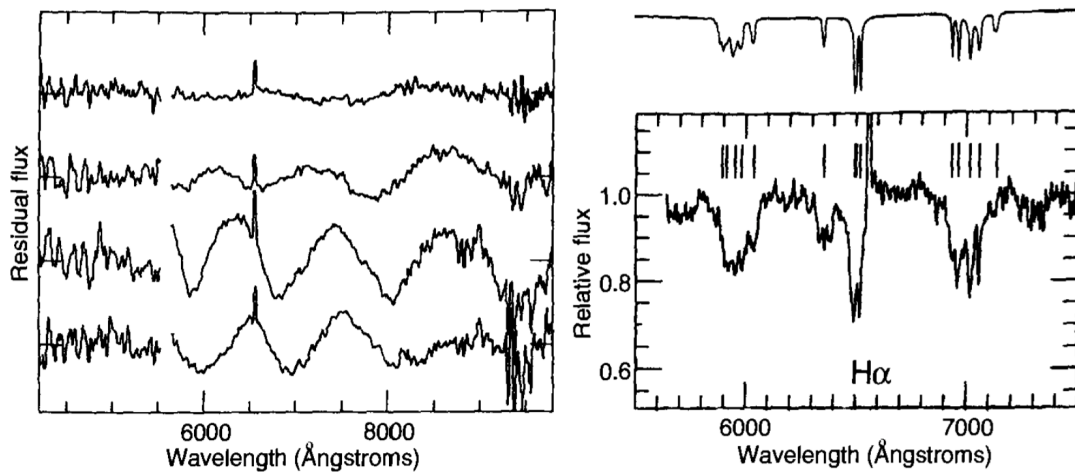
Figure 1.14: Left: The cyclotron humps in MR Ser vary dramatically over the orbital phase since the viewing angle of the accretion region varies. The four spectra are from phases 0.41, 0.50, 0.58, and 0.67 from bottom to top, respectively. The data were taken in a low state and are shown after subtraction of a smooth continuum. The narrow line is Hα emission from the secondary. Right: Higher-resolution spectra reveal multiple Zeeman-split components of the Hα absorption from the white-dwarf surface. The individual components are marked by vertical lines, while a model Zeeman spectrum is shown above. Both the cyclotron humps and the degree of Zeeman splitting indicate a field strength of 28 MG. (Source: Coel Hellier)

1.3.6 Polarisation of Cyclotron Emissions

Polarization refers to the orientation of the electric field, and by extension, the magnetic field present in the photons. Polarized light has the fields of each photon aligned in the same direction with respect to other photons. The cyclotron emissions have both linear circular polarization.

The linear polarization can be explained by looking at the magnetic field lines of the system side-on. Upon inspection, we see that the particles which are moving as a cyclotron appear to be coming in and out of the plane in areas on either side of the field line. This motion leads to light that is linearly polarized as its electric field is in the direction of this oscillation.

The circular polarization is apparent when we look along the magnetic field lines we see only the circular motion of particles, thus the electric field follows that rotation and results in circular polarization. When viewing the system at an angle different from those described above for polarization, we get a mixture of circular and linear polarization in the light received, this mixture directly determines the angle at which the system is seen.

1.3.7 Accretion Region

The region of accretion is stretched out in an area around the magnetic poles due to the varying density of material hitting it. The varying densities also cause different frequencies of radiation to be emitted from the poles. As the mist hits the poles, its kinetic energy is converted into thermal energy and releases copious amounts of hard X-rays.
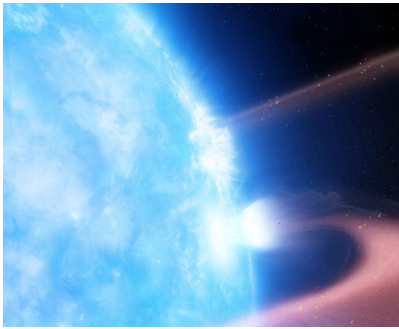
Figure 1.15: Accretion region (Source: Mark A. Garlick)

These particles also collect on top of the star and form a protrusion about $0.1R_{wd}$ in height. The heavier material, however, does not convert its kinetic energy to thermal energy and instead plunges straight into the star, thereby emitting soft X-rays instead.

Diffused material is funneled by field lines into a 20-keV accretion shock some distance from the magnetic pole, X. We see hard X-rays from the post-shock region and softer X-rays from the surrounding region, heated to 20 eV by radiation from the shock (Figure:1.16). Electrons spiraling down the field lines also produce cyclotron emissions. On the right, denser blobs of material plough deep into the white dwarf atmosphere, heating a region to soft-X-ray temperatures.

1.3.8 Accretion States

The high and low accretion states in Magnetic Cataclysmic Variables (MCVs) correspond to varying levels of mass transfer and accretion rate onto the white dwarf, resulting in distinct levels of brightness and activity in the system.

During the high accretion state, the rate of accretion is significantly elevated, leading to frequent and intense X-ray outbursts and emissions in the optical and ultraviolet spectra. This heightened activity makes the MCVs appear much brighter and more active compared to the low accretion state. Additionally, the white dwarf may experience magnetic flares, generating

Figure 1.16: A schematic AM Her accretion region (Source: Coel Hellier)

strong magnetic fields that contribute to further fluctuations in the emitted radiation.

An outburst takes place when the accretion rate experiences a sudden and dramatic increase. During an outburst, the system's brightness can surge by several magnitudes, surpassing its usual luminosity. Such occurrences can be triggered by various factors, including temporary enhancements in mass transfer from the companion star, the buildup of material in the outer regions of the accretion disk, or instabilities within the accretion process itself. This leads to intense X-ray emissions and other electromagnetic radiation across various wavelengths, making the MCV exceptionally radiant. Investigating these outbursts offers valuable insights into the dynamics of accretion, the role of the white dwarf's magnetic field, and the intricate interactions within these binary star systems.

In contrast, during the low accretion state, the emission of X-rays and other radiation from the MCV decreases. Consequently, the system appears fainter and exhibits reduced overall activity. Although the white dwarf's magnetic field may
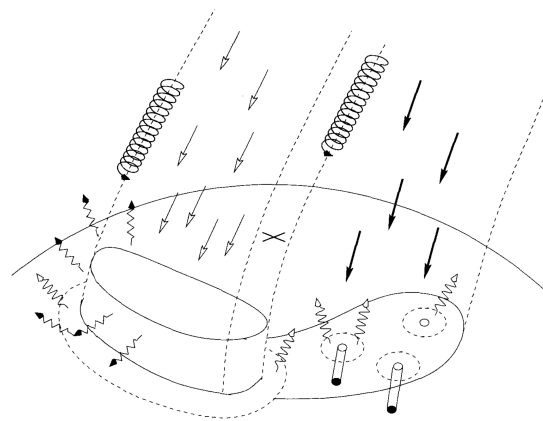
still be present, it exerts less energetic influence during this state.

The transition between the high and low accretion states is often accompanied by changes in the system's brightness and emission characteristics. These transitions can occur over timescales spanning from days to months, and the exact mechanisms driving these variations remain an active area of research in astrophysics.

1.3.9 Accretion Modes

There are two types of accretion modes: Single-Pole and Double-pole accretion. In single-pole accretion, the material from the companion star is channeled and accreted onto only one magnetic pole of the white dwarf. This concentrated stream of material impacts the white dwarf's surface near the magnetic pole, resulting in a localized hotspot of high temperature and intense radiation.

Unlike single-pole accretion, in which material is funneled onto a single magnetic pole, in double-pole accretion, there are two accretion spots, one on each magnetic pole. The material from the companion star is funneled along the magnetic field lines to these two poles, creating two localized hotspots on the white dwarf's surface. With double pole accretion, the observed emissions from the system are more evenly distributed around the white dwarf. As the white dwarf and the companion star orbit each other, the two hotspots rotate in and out of view, leading to periodic changes in brightness and emissions.

The distribution of accretion spots on the white dwarf's surface affects the system's overall brightness, the patterns of variability, and the characteristics of the emitted radiation.
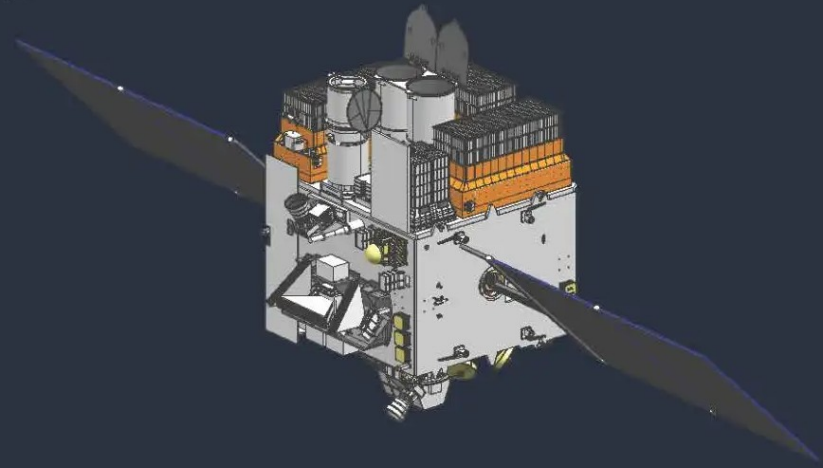
2. Instrumentation and Methodology

2.1 Astrosat and UVIT

2.1.1 Astrosat - India's first multiwavelength space telescope

AstroSat is the first dedicated Indian astronomy mission aimed at studying celestial sources in X-ray, optical, and UV spectral bands simultaneously. The payloads cover the energy bands of Ultraviolet (Near and Far), limited optical and X-ray regime (0.3 keV to 100 keV). One of the unique features of the AstroSat mission is that it enables the simultaneous multi-wavelength observations of various astronomical objects with a single satellite.

AstroSat with a lift-off mass of 1515 kg was launched on September 28, 2015, into a 650 km orbit inclined at an angle of 6 deg to the equator by PSLV-C30 from Satish Dhawan Space Centre, Sriharikota. The minimum useful life of the AstroSat mission is expected to be 5 years.
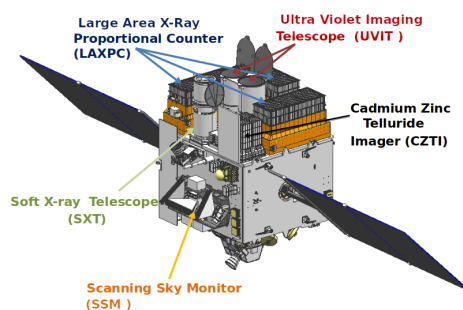
Figure 2.1: Various Payloads on Astrosat (Source: ISSDC)

The spacecraft control centre at Mission Operations Complex (MOX) of ISRO Telemetry, Tracking and Command Network (ISTRAC), Bengaluru manages the satellite during its entire mission life. The science data gathered by five payloads of AstroSat are telemetered to the ground station at MOX. The data is then processed, archived, and distributed by Indian Space Science Data Centre (ISSDC) located at Bylalu, near Bengaluru.

2.1.2 Ultra-Violet Imaging Telescope (UVIT)

The Ultra Violet Imaging Telescope (UVIT) is one of the five payloads onboard the AstroSat Satellite, designed to conduct surveys of the Visible, Far Ultra Violet, and Near Ultra Violet bands in the sky. Its primary objective is to simultaneously capture images of a specific region of the sky using three channels: FUV (Far Ultra Violet, 130-180 nm), NUV (Near Ultra Violet, 200-300 nm), and VIS (Visible, 320-550 nm). This enables UVIT to observe and study various celestial objects such as stars, galaxies, and other bright UV sources (Tandon et al., 2017).

UVIT utilizes two identical co-aligned telescopes (T1 and T2) which are configured in a Ritchey-Chretien setup, covering a field of ~28 arc-minutes. These telescopes collect radiation from the target region and transmit it to the detector system via a filter wheel which is employed to allow for the selection of different filters. For both the FUV and NUV channels, multiple filters are available to facilitate observations within narrower wavelength bands. Additionally, UVIT offers the option of slitless spectroscopy, enabling the study of objects with a resolution of ~80.

Instrumentation

As mentioned previously UVIT consists of two Ritchey-Chretien Telescopes (Aperture ~375mm); one of these makes images in FUV and the other makes images in NUV and VIS; the radiation is divided orthogonally between NUV and VIS channels by a dichroic beam splitter. Radiation from off-axis sources attenuates through a cylindrical baffle and light eventually reaches the detectors (Intensified Complementary Metal Oxide Semiconductor Imagers or CMOS). The CMOS imagers have 512×512 pixels, and each of these pixels is mapped to 8×8 subpixels in the final image to get a plate scale of ~0.416 arc-second per pixel. These detectors can be used in Photon Counting mode (High intensification/gain) or Integration mode (Low intensification/gain) to get a resolution of 1.8 arc-second FWHM (Tandon et al., 2020).
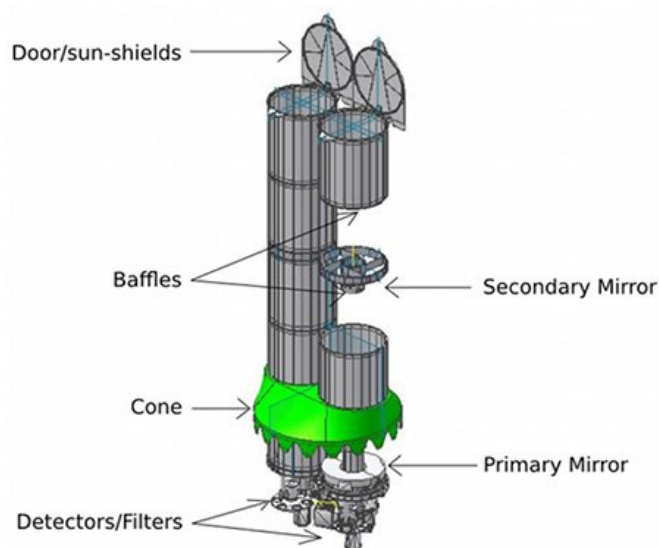

Figure 2.2: UVIT Payload Structure (Source: IIAP)

A photon is detected after an incident UV/optical photon ejects a primary electron from the Photo-Cathode, which is accelerated towards and multiplied within the Micro-Channel-Plate (MCP). These electrons are then accelerated towards the Anode (Phosphor coating) which is read out as a photon event in the CMOS imager.

To protect the detectors from intense radiation, AstroSat oscillates its pointing on orthogonal UVIT image axes at the rate of a few arc seconds per second with an amplitude of a few arc minutes.

Calibration

Pixel-based readouts on the CMOS imager introduce systematic errors in the centroiding and counting of photon events, requiring the calibration of images. A detailed description of these calibrations is provided in Tandon et al., but broadly, there are five sets of calibration steps:

1. Photometric Calibration:
   - Zero-Point Magnitudes: The reference HZ 4 is used to calculate zero-point (ZP) magnitudes, which serve as a measure of detector sensitivity.
   - Flat-Field Variations: Spatial variations in detector sensitivity are estimated using exposures taken for three fields in the Small Magellanic Cloud (SMC).
   - Saturation Corrections: Saturation occurs when two or more photons occur in close proximity, erroneously recorded as a single photon event.
2. Sensitivity monitoring of the FUV and NUV channels: UV optics are highly sensitive to molecular contaminations, and systematic errors can also arise from aging filters, MCPs, and optical element coatings. Regular monitoring is conducted to address these issues.
3. Spectral calibration for FUV and NUV gratings: This step involves calculating and estimating dispersion, effective area as a function of wavelength, and resolution.
4. Approximation of the Point-Spread Function (PSF): The PSF describes the spreading or blurring of an ideal point source over an image. It consists of a narrow core and an extended pedestal, including encircling energy as a function of radius.
5. Astrometric calibrations: These calibrations are necessary to address incorrect measurements or deviations in the positions of light sources, which can arise from optical and other distortions.

Parameter	FUV	NUV	VIS
Wavelength ()	1300–1800	2000–3000	3200–5500
Mean wavelength ()	1481	2418	4200
Mean effective area (cm^2)	$\sim$10	$\sim$40	$\sim$50
Field of view (diameter—arcmin)	28	28	28
Plate scale (arc second/pixel)	3.33	3.33	3.30
Astrometric accuracy (rms)	0".4	0".4	-
Zero-point magnitude	18.1	19.8	-
Spatial resolution (FWHM)	1".3 - 1".5	1".2 - 1".4	2".5
Spectral resolution (Å)	17	33	-
Saturation (counts/s)	6	6	-

Table 2.1: *Key Parameters of the Three Channels of UVIT*

2.2 Image Reduction

The first part of our study involved gathering data from the UVIT and imaging the systems under study. This was done to help locate the system of interest in the field and gather details about certain properties like the surface brightness profile. The data comes in the form of fits images and was reduced using CCDLAB — a software developed for UVIT data reduction. Being a specialized program, most of the data reduction procedure is heavily automated. Detailed pipelines of UVIT data reduction using CCDLAB are available (Postma and Leahy, 2021), but a brief summary of the steps followed in order to image the systems under study are presented below.

1. UVIT L1 data for the system under study was downloaded from the Astrosat archive by entering the name of the system under the "Search" tab, resolving by NED/SIMBAD and selecting the UVIT instrument.
2. CCDLab and 7Zip were installed and UVIT calibration files were downloaded from the GitHub page. The calibration files were moved to the C drive (as required by CCDLAB)
3. On CCDLAB, the "Extract L1 gz or zip archives" option was used, and the zip file containing L1 data was selected
4. The software tries to automatically extract the files and apply drift correction.
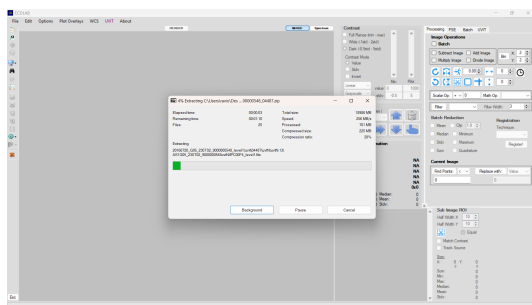

(a) Extracting L1 files
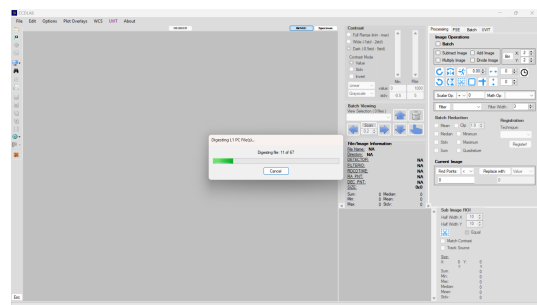
(b) Digesting the files

Figure 2.3: Some of the steps involved in processing the images

5. In some cases, automatic drift correction using INT mode frames did not work because of noise in the images. Here, drift correction was instead performed manually by selecting bright sources that stayed within the frame of the image for the duration of the particular observation (regular prompts are provided by CCDLAB)
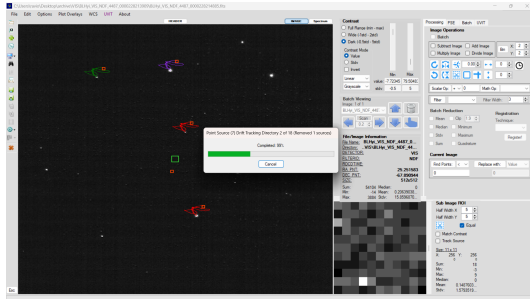
(a) Drift correction being applied

(b) An example of an erroneous file with too much drift during exposure

Figure 2.4: Drift

6. Erroneous files with blank images, noise, motion blur, or other artifacts were deleted.
7. The FUV and NUV images were then stacked by registering bright objects as references.
8. This was done using the "General Registration" option under the "Registration, Transformation, Merge" option.
9. After registering one source to correct for relative translational motion of the sensor and another to correct rotation between frames, the "Merge Centroid Lists" option was used to merge all the images into two files - one FUV and one NUV file
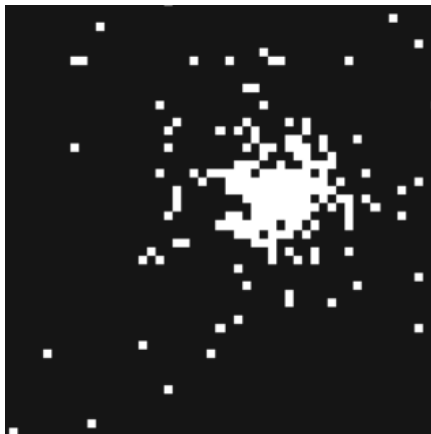

(a) Before stacking

(b) After stacking and smoothing

Figure 2.5: Comparison of the same source before and after stacking

10. The "Solve" option was used under the "Auto WCS" section to solve for WCS coordinates. Once again, in some cases where the sources were too faint to automatically solve for the WCS, the process was performed manually by using SIMBAD as a reference to enter the coordinates of at least three bright sources in the frame of the image.
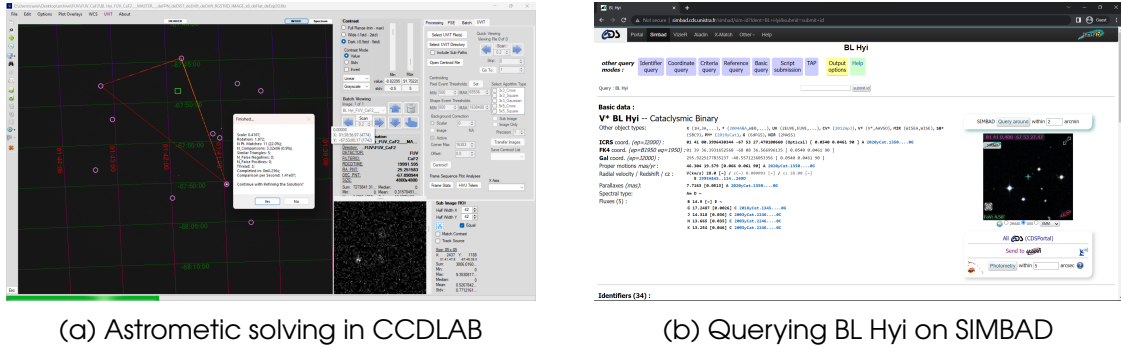
(a) Astrometic solving in CCDLAB   (b) Querying BL Hyi on SIMBAD

Figure 2.6: Solving and Verifying the Astrometry

11. The WCS solution was verified using a star chart generated on a variable star plotter and using the star map on SIMBAD. The patterns seemed to match indicating the WCS co-ordinates were correctly solved for.

2.2.1 Image Analysis — Surface Brightness Profile

Once the final science images were generated, a variety of analyses could be performed on them to obtain more information about the source. One such method of analysis is the surface brightness profile. The surface brightness profile of a source helps characterize the source and distinguishes point sources from extended sources. Point sources, like the cataclysmic variables under study, ideally have a brightness distribution resembling a delta function — with a peak at the center of the source and a null reading everywhere else. Since we are working with instruments prone to some errors, we expect a Gaussian distribution from the source, with a peak at the center and a sharp dip moving away. This was done using SAOImageDS9 - a FITS image visualization tool made for astronomical images (Smithsonian Astrophysical Observatory, 2000).

The procedure for plotting the surface brightness profile is detailed below:
1. The finalized image was opened on SAOImageDS9 and options in the "Scale" tab were adjusted to make the source clear and visible.
2. Under the "Region" tab, annuli were generated, centered at the source. Annuli are used to average out the circumferential variation of brightness and only account for radial changes.
3. Around 10-15 annuli (more concentrated near the center) were generated and spread out until the brightness started to even out.
4. The brightness data was then exported and a graph of the count rate against the average radius was plotted.
5. An output half-Gaussian shape was used to confirm that the sources were indeed point sources.
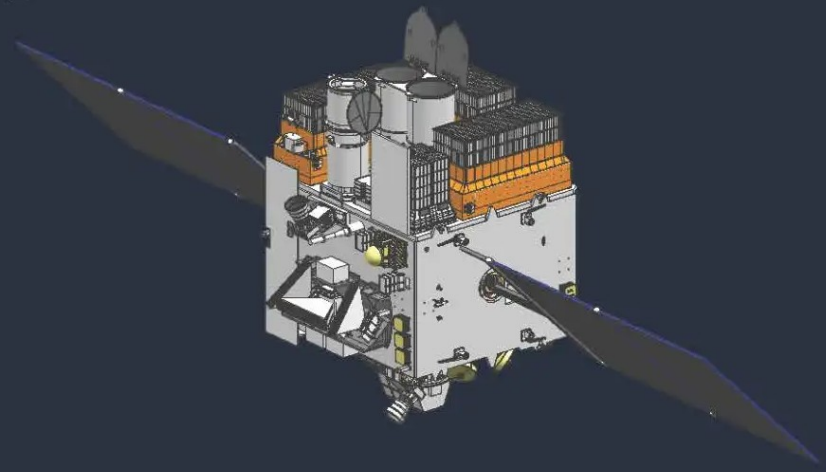
3. Temporal Analysis

The next part of the study involved analyzing temporal variations of the systems under study. To do so, ASTROSAT's UVIT L2 data was obtained from the ASTROSAT archive and analysis was conducted using Python.

3.1 Light Curves

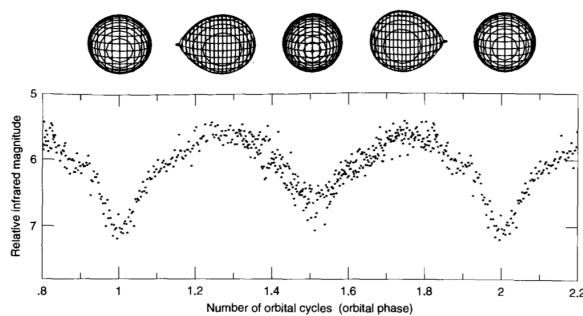Plotting the light curve of a binary can show useful information about its Roche lobe and orbital period.

Figure 3.1: Light-curve of a Binary System (Source: Coel Hellier)

The figure on the left shows how the light curve is formed for a binary cataclysmic system. The Roche lobe comes in and out of view, thus increasing and decreasing the flux seen by us respectively. Note that this kind of light curve is only possible in the case of systems seen from their side (edge-on view). No variation in the light curve would be noticed when viewed along its rotation axis (top-down).

3.1.1 Generating light curves

Creating light curves for the systems was the initial step in the temporal study. This step helps ascertain any apparent temporal variations in the data and helps to validate the L2 data (data that shows a constant decrease or increase over time might need to be discarded). The light curve can then be studied further to understand the properties of the system, like its orbital period, accretion state, and magnitude and flux variation.

The procedure that was used to generate light curves is as follows:

1. The system was located in each of the FUV and NUV orbits in the instrument coordinate using a FITS image viewer like SAOImageDS9 or CCDLab. The image file in the instrument coordinate will have a file name ending with '*l_l2img.fits'
2. The Curvit package was installed and the curves function was used to generate .dat files containing the count rate variations over time.
3. The .dat files from all the orbits were merged and plotted to make the light curve

3.1.2 Plotting the power spectrum and folding

Most light curves plotted don't show an obvious period as the data is very crowded with some noise within. In order to find the most common period within the data, a periodogram is plotted. A periodogram is a variation of the Fourier transform that shows the relation between the period and its relative contribution (power) to the time series. The data from the UVIT is unevenly sampled with gaps. Hence, Lomb–Scargle periodogram algorithm is used in order to find the period of the system (VanderPlas, 2018).

This was done using the LombScargle class from the astropy.timeseries package on Python. Once the periodogram was generated and plotted, the orbital period is confirmed by looking for a frequency (ω) with high power and whose harmonics ($2\omega, 3\omega$ etc.) are also clearly visible in the power spectrum.

Folding

Once the orbital period is obtained, the data can be 'folded' onto the orbital period to analyze the variation within different phases of an orbit. This is done by first converting the time of observation to the orbital phase in the following way:

$$\phi = \frac{t - t_0}{P_{orb}}$$

where ϕ is the orbital phase, t is the time of observation, t_0 is the epoch (time when the system was first observed) and P_{orb} is the orbital period of the system. (refer: Variable Star Astronomy by AAVSO (Mattei and Percy, 1999)) As the variable star system's brightness is known to have a cyclical pattern, a phase of ϕ is equivalent to a phase of $n + \phi$ where $n \in \mathbb{Z}$. All the equivalent phases can then be combined by taking a modulus with 1. This when plotted gives us the phase folded light curve.

Binning

When the light curve is phase folded, points get concentrated and the graph starts to get cluttered making it more difficult to analyse. To resolve this, the data is binned into set intervals of phases and averaged before plotting.

4. AR UMa

4.1 Introduction

AR UMa[1] was first identified by the Einstein Slew Survey as a bright X-ray and Optical source (Remillard et al., 1994). Present in the constellation Ursae Majoris, AR UMa is the most strongly Magnetic Cataclysmic Variable observed until now with magnetic fields getting as strong as ~230 MG. Accreting binaries, such as AR UMa itself, containing a highly magnetic white dwarf are called Polars or AM Her systems. It has been observed that AR UMa spends most of its time in a state of low accretion, V ~ 16.5 (Vega Magnitude), with sporadic high states that reach up to V ~ 13.5 (Schmidt et al. (1996)). When in high states, AR UMa also emits strongly in the UV regime. Other important parameters are described in Table 4.1 below.

Target	AR UMa
Type	AM Her CV
RA(α, FK5 in Degrees)	168.9360046
Dec(δ, FK5 in Degrees)	42.97299957
Parallax(mas)	10.1182
Distance(pc)	~ 88
Period(hr)	1.932

Table 4.1: *Parameters of AR UMa (Source: Simbad and Schmidt et al. (1996))*

4.2 Description

4.2.1 Flux

Flux, also known as apparent brightness, refers to the total amount of light energy that passes through a unit area of our telescope. Measuring the flux is crucial as it provides a fundamental basis for estimating the intrinsic properties of celestial objects, such as the surface temperatures within our system. The flux of AR UMa is really high in soft X-rays, UV, and optical regions (Table 4.2).

---

[1]Studied by Sparsh Gupta

Wavelength	Flux	Equivalent Width
(Å)	(10^{-13} ergs cm^{-2} s^{-1})	(Å)
1239 + 1243	7.9	39
1300	0.9	5
1334	2.1	11
1393 + 1402	6.2	26
1548 + 1550	26.1	152
1640	6.3	45

Table 4.2: *High-State Flux in UV regime for AR UMa (Schmidt et al. (1996))*

4.2.2 Accretion States

AR UMa has extended low states with a duration ranging from months to years along with irregular high states (Table 4.3). The extended low-state has allowed us to calculate the orbital period whereas high-state observations give us better insight into the system's geometry due to the high luminosity of the system at the time.

Date (YYYY:MM:DD)	Telescope/Observatory	Accretion State
1998:11:14	SO (2.3m)	Low
1998:05:22	SO (2.3m)	Low
1998:04:01	SO (2.3m)	Low
1997:12:05	SO (2.3m)	Low
1997:04:03	SO (2.3m)	Low
1997:03:04	APO	Low
1997:02:02	LO (1.8m)	Low
1997:01:22	MMT	Mid
1996:12:27	LO (1.8m)	High
1996:12:19	Braeside	High
1996:12:17	Mount Laguna	High
1996:12:16	Braeside	High
1996:12:14	EUVE	High
1996:12:13	Braeside	High
1996:12:08	SO (2.3m)	High
1996:12:07	SO (2.3m)	Mid
1996:12:03	SO (2.3m)	Low
1996:04:28	MRO	Low
1996:04:27	ASCA	Low
1996:03:16	SO (2.3m)	Low
1996:01:27	SO (2.3m)	Low
1995:12:15	IUE	Low
1995:11:23	SO (1.5m)	Low
1995:10:25	SO (1.5m)	High
1995:05:05	OAN (1.5m)	High
1995:04:12	IUE	High
1995:04:06	OAN (1.5m)	High

Table 4.3: *Low/High-States of AR UMa (Source: Szkody et al. (1999) and Schmidt et al. (1996, 1999))*

4.3 Image Processing and Analysis

4.3.1 Creating Master Images

After extracting and digesting L1 files into CCDLAB, our next step is to generate finalized master images that can be utilized for scientific analysis on the system. Following the corrections described in Section 2.2, the images were merged and stacked to produce two FITS Master images for the corresponding filters (Fig 4.1). A statistical overview of the telescope observations is given in the table below.

Target	Instrument	Start Time (UT)	Stop Time (UT)	Exposure (s)
AR UMa	AstroSat FUV (F3 or F169M)	2016:05:22:06:09	2016:05:26:14:08	44761.35
(Obs. ID - G05_045T01_9000000468)	Astrosat NUV (F5 or N263M)	2016:05:22:06:09	2016:05:26:14:08	45835.905

Table 4.4: *Details of UVIT observations of AR UMa*

(a) Raw L1 FUV Image

(b) Raw L1 NUV Image

(c) Master FITS FUV Image (Stacked)
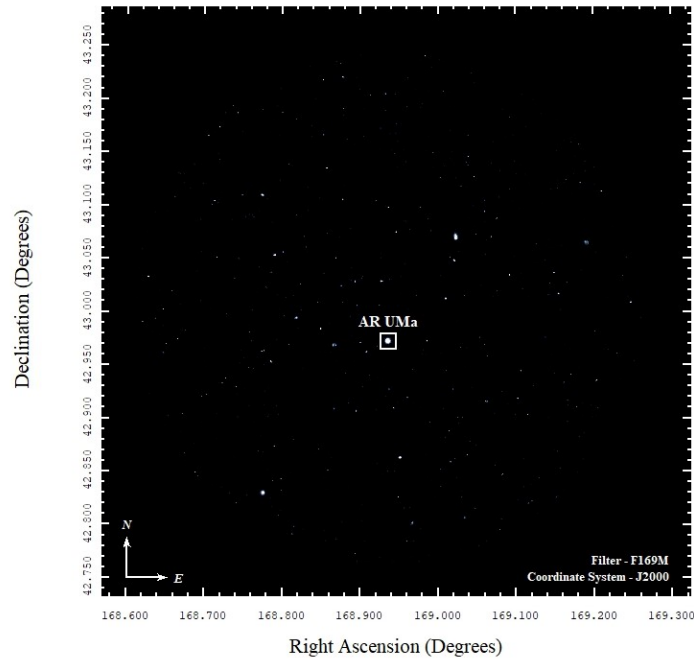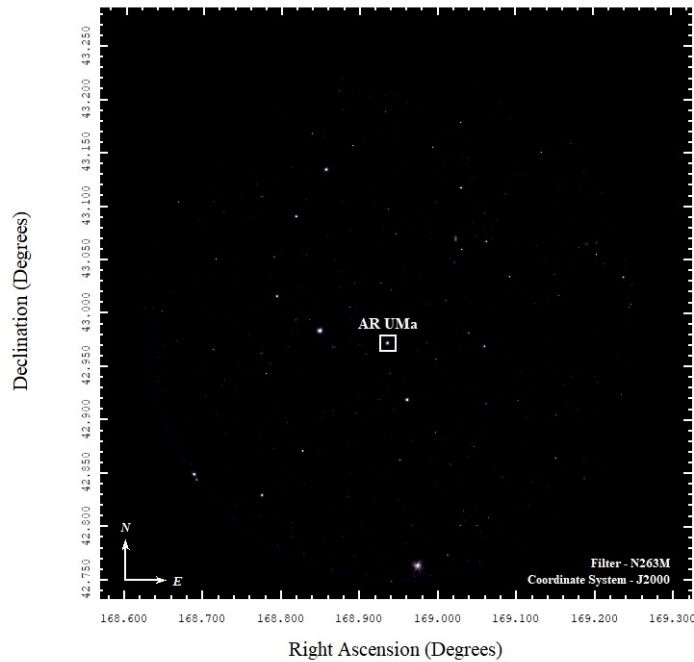

(d) Master FITS NUV Image (Stacked)
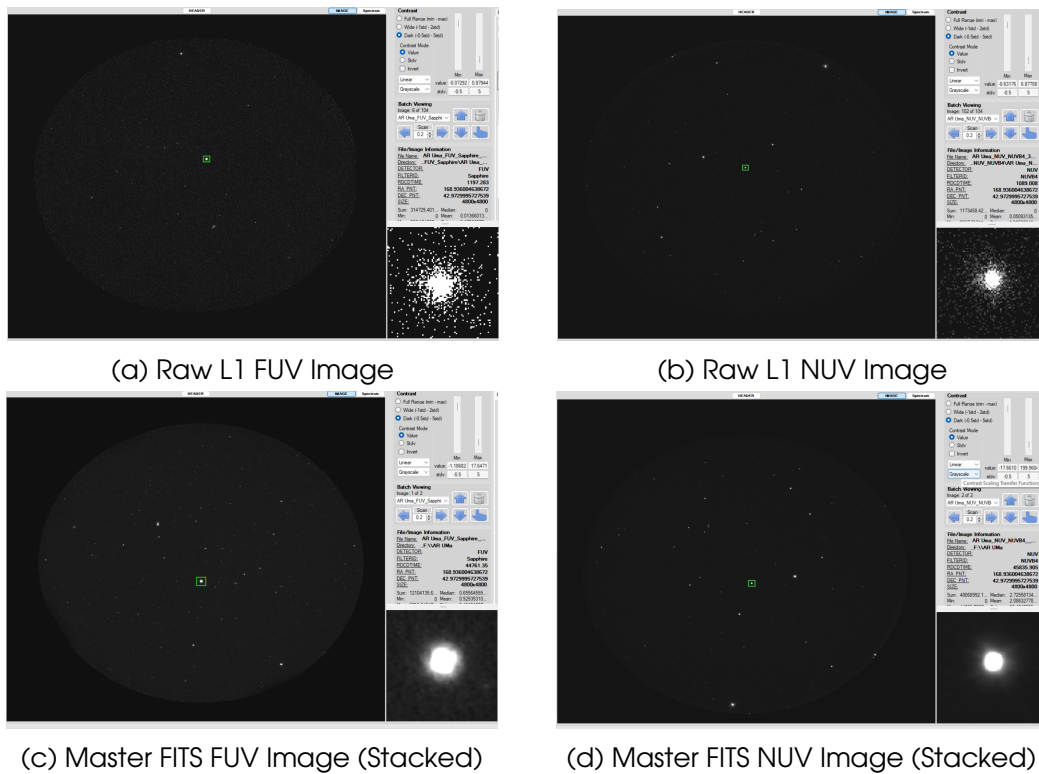
Figure 4.1: *Raw and Stacked FUV and NUV data of AR UMa*

4.3.2 Final Scientific Images

The final scientific images (Fig 4.2) were created and exported using SAOImageDS9 which is a widely used astronomical imaging and data visualization software. The images were exported in two formats; JPEG and EPS.
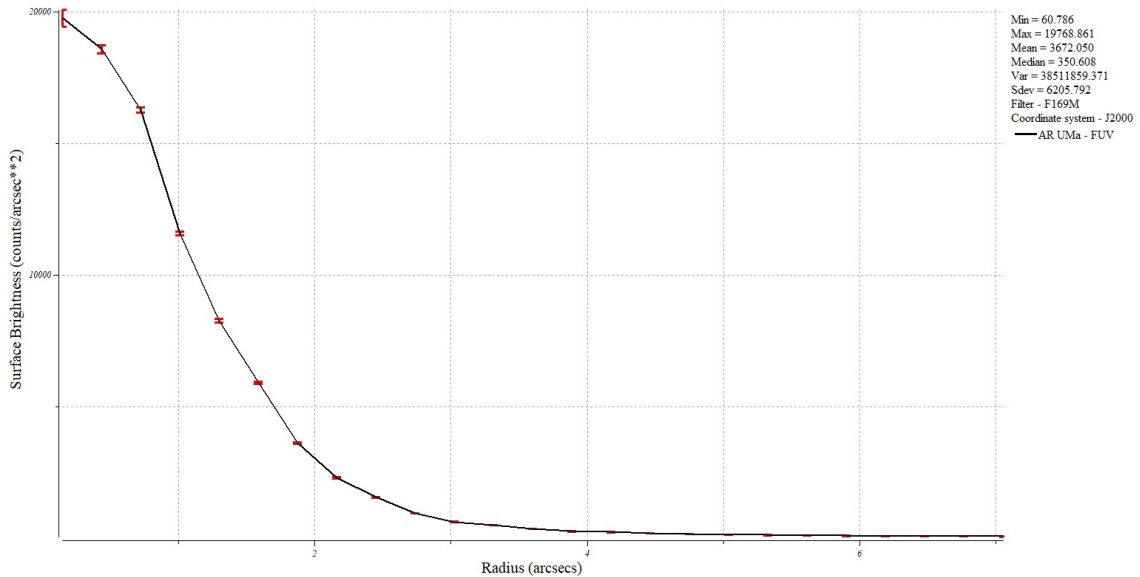

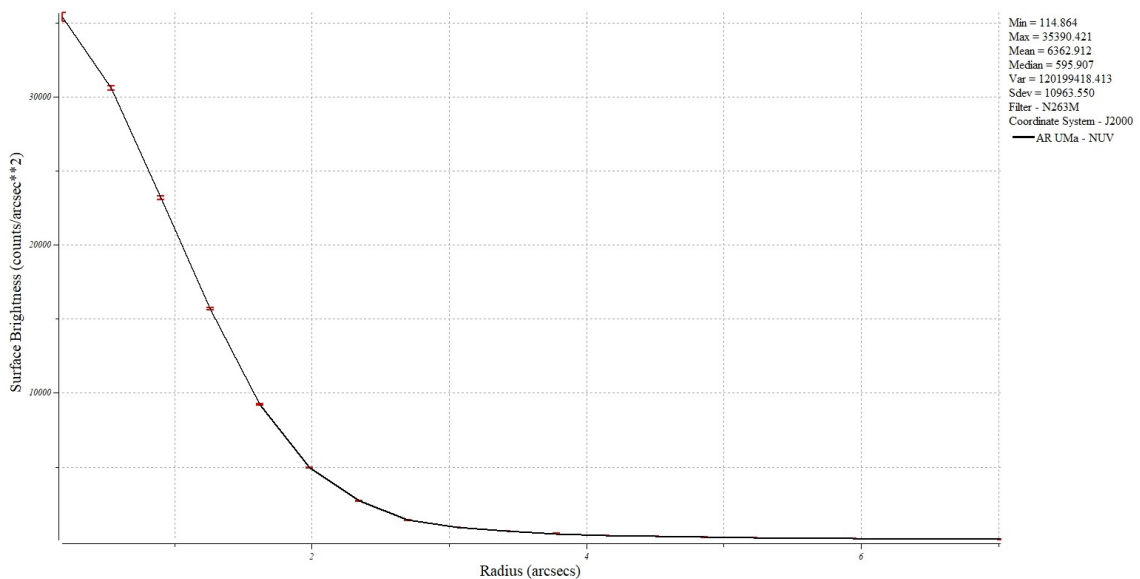(a) Final FUV Image

(b) Final NUV Image

Figure 4.2: *Final Science Images of AR UMa*

4.3.3 Surface Brightness Profile

A surface brightness plot provides an estimation of how brightness changes with respect to the radius. These plots are generated by creating Annuli regions on the system, which is a feature available in DS9.


(a) FUV Radial Profile

(b) NUV Radial Profile

Figure 4.3: *Surface Brightness plots of AR UMa*

Based on the clear observations from these plots, we can conclude that the source is a point source rather than an extended source. This conclusion is supported by the fact that the plots exhibit a Gaussian distribution pattern.

4.4   Temporal Analysis

After extracting the L2 data, a time-series analysis is performed by generating a light curve, illustrating the variation of photon count rate over time. The resulting plots for both filters are presented below.
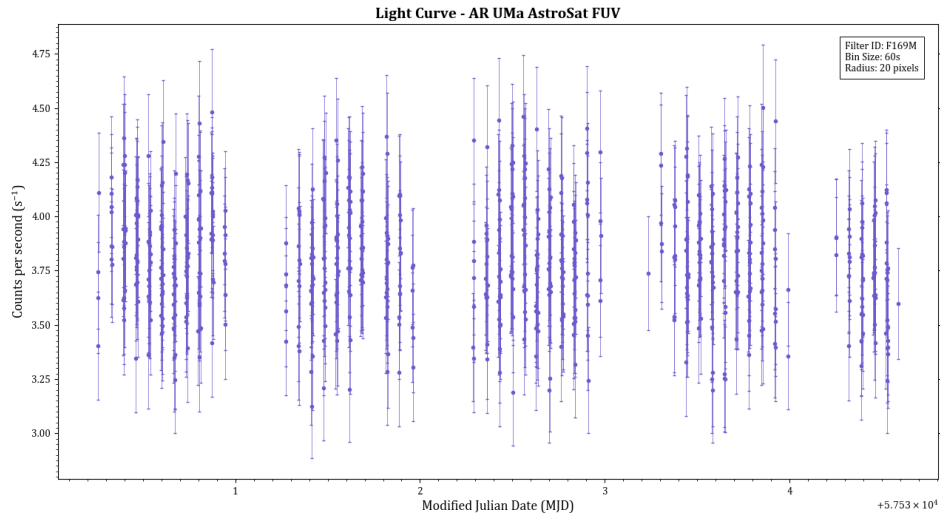
(a) FUV, Mean Count Rate = 3.80 s^{-1}
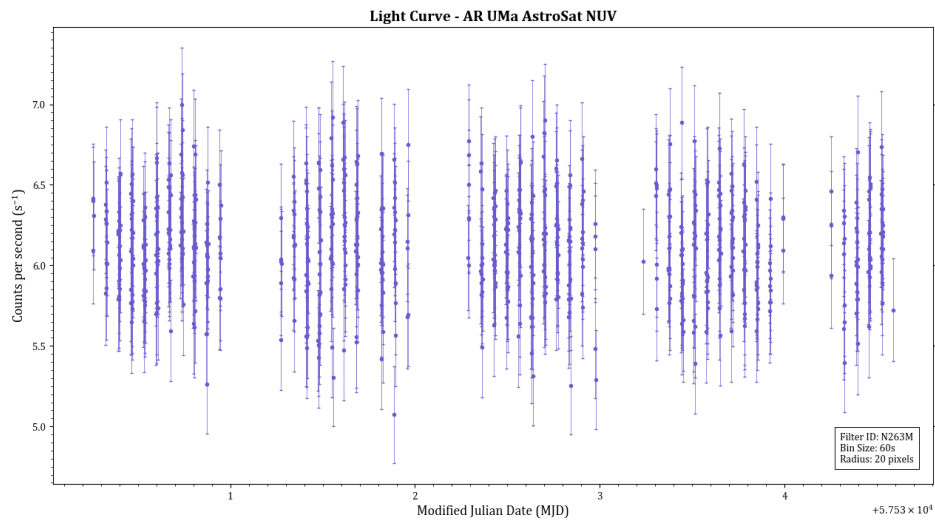
(b) NUV, Mean Count Rate = 6.11 s^{-1}

Figure 4.4: *Light Curves of AR UMa derived from the L2 data*

We may convert the count rate into flux using the conversion value mentioned for the filter on the ASTROSAT UVIT website).

Filter ID	Unit Conversion	Mean count rate (s^{-1})	Flux (ergs cm^{-1} s^{-2} Å^{-1})
F169M	4.392×10^{-15}	3.80	1.6689×10^{-14}
N263M	0.844×10^{-15}	6.11	5.1568×10^{-15}

Through extensive observations, it has been inferred that AR UMa predominantly remains in a Low Accretion state, with high accretion events being rare occurrences. The UV spectral energy distribution for one such low state can be found in Hoard et al., which provides a summary of the flux values across a range of wavelengths while the system is in a low state. Our FUV Filter: F169M has a mean wavelength of 1608 Å, and the NUV Filter: N263M has a mean wavelength of 1717 Å. Upon examination of these wavelengths in Fig 4.5, we find that our recorded flux values align with the characteristics indicative of AR UMa being in a low state. Consequently, it can be deduced that during our observation period, AR UMa was in its low accretion state.
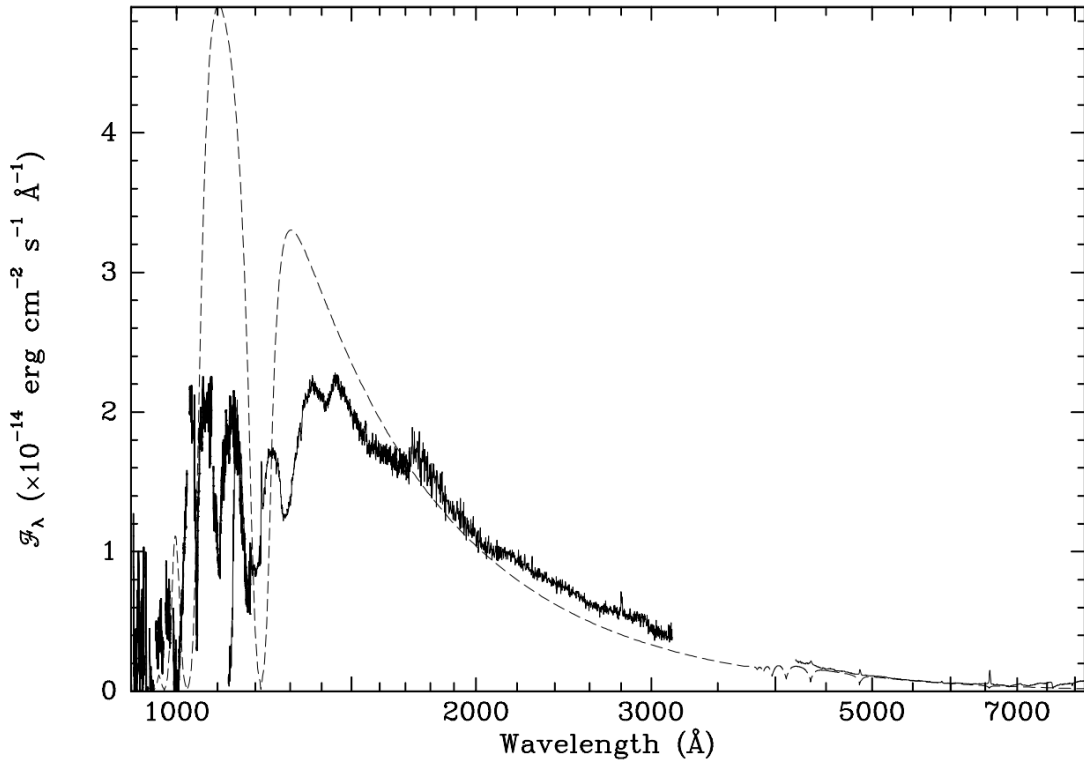

Figure 4.5: *AR UMa UV-optical Spectral Energy Distribution (Source: Hoard et al. (2004))*

In order to determine the orbital period of the system, Lomb-Scargle Periodograms were generated, which provided us with insights into the dominant frequencies present in the light curve.

Fig 4.6 reveal orbital periods of 1.9331 hrs and 1.9318 hrs, respectively for FUV and NUV, as obtained from the Lomb-Scargle Periodograms. These values are in close agreement with the actual orbital period of 1.932 hrs reported in Schmidt et al. (1996), suggesting consistency between our analysis and the existing literature. The minor variations in the derived periods could be attributed to uncertainties in the data or the sensitivity of the analysis method.
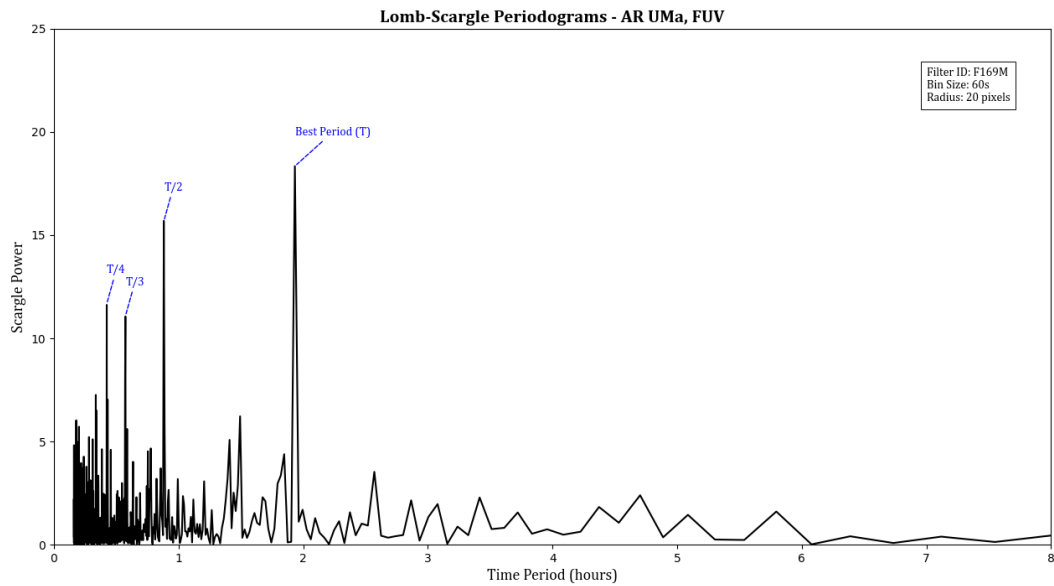
(a) FUV, T = 1.9331 hrs
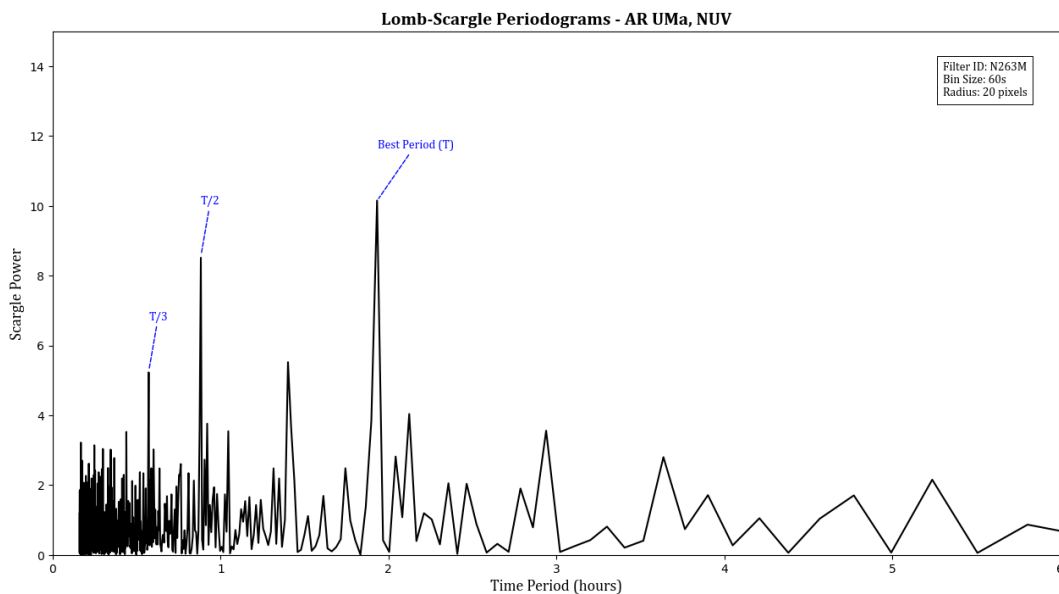
(b) NUV, T = 1.9318 hrs

Figure 4.6: *Lomb-Scargle Periodogram for AR UMa's orbital period*

To observe the Flux variation and determine the accretion mode for AR UMa, the light curve was folded and binned utilizing the ephemeris provided in Schmidt et al. (1999). This approach allowed us to correct for the phase and align the data points appropriately. By doing so, we were able to enhance the clarity of the accretion pattern.
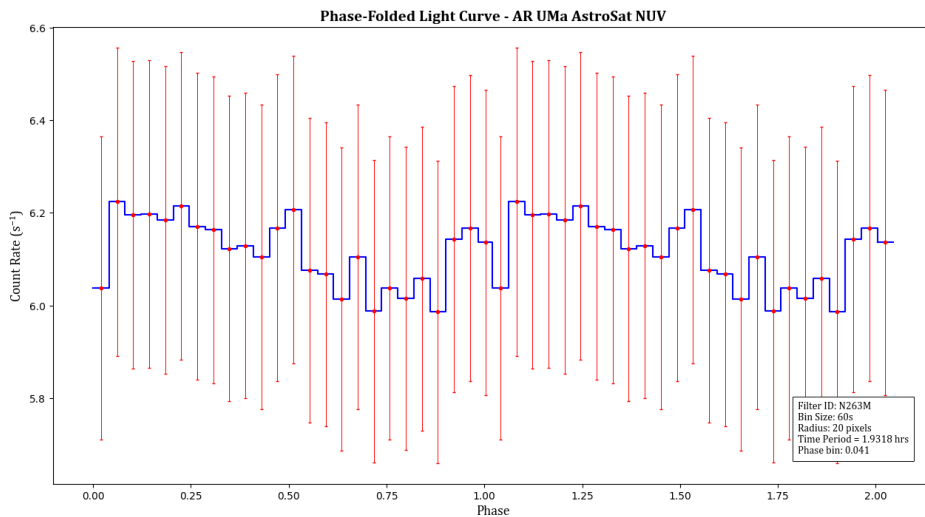
$$\text{Ephemeris: } HJD = 2450470.4309(5) + 0.08050074(12)E$$

$$\text{Flux } f_\lambda \text{ (in ergs cm}^{-2}\text{s}^{-1}\text{Å}^{-1}) = \text{Count Rate} \times \text{UC}$$

$$UC = 4.392 \times 10^{-15} \text{ for F169M; } UC = 0.844 \times 10^{-15} \text{ for N263M}$$
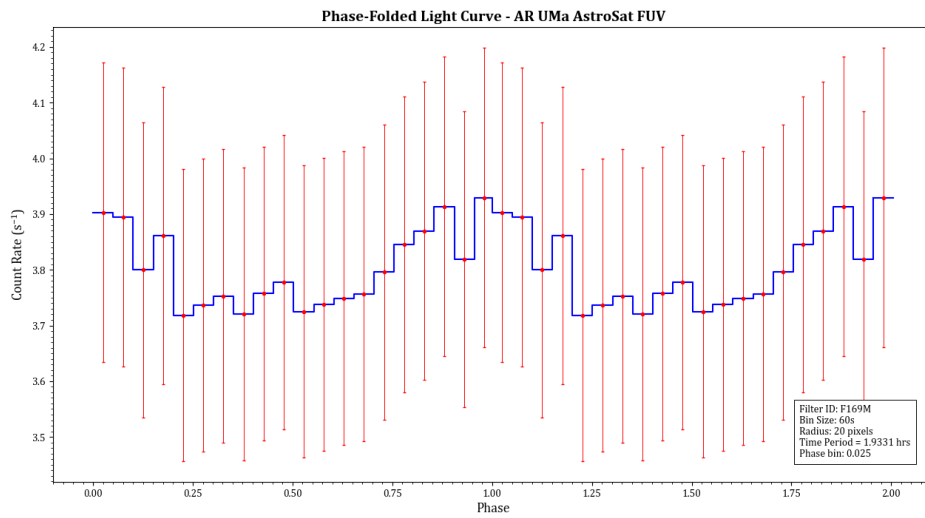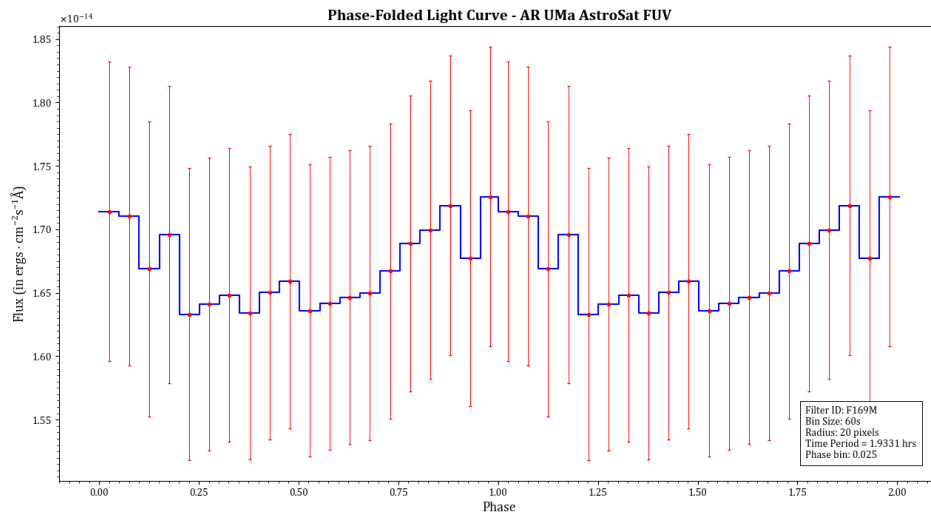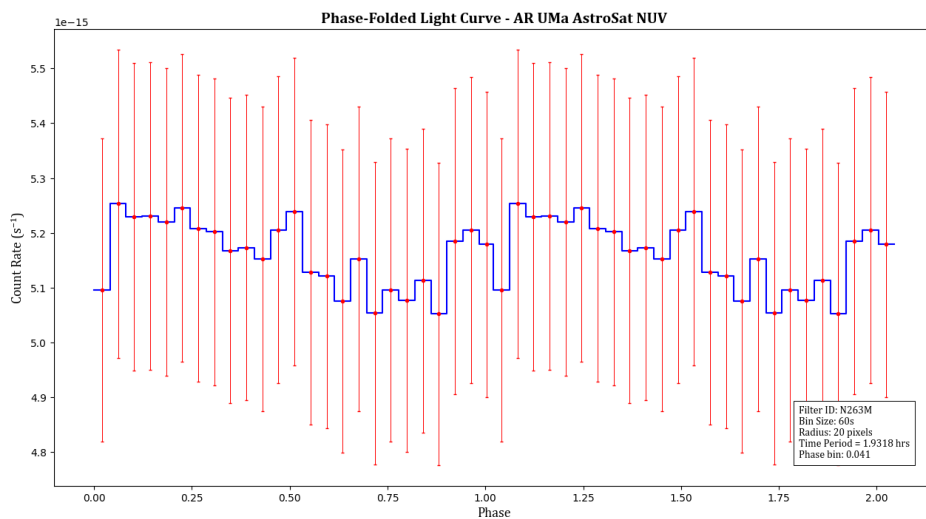

(a) Count Rate vs Time for FUV

(b) Count Rate vs Time for NUV

Figure 4.7: *Binned- Phase Folded Lightcurves for AR UMa*

(a) Flux vs Time for FUV

(b) Flux vs Time for NUV

Figure 4.8: *Binned- Phase Folded Lightcurves for AR UMa*

The binned phase-folded light curves indicate the presence of a two-pole accretion mode, as evidenced by the presence of two periodic peaks at approximately phase 0.50 and 1.50, respectively. Although the FUV light curve shows a smaller peak, it is still discernible. Additionally, the fact that our phase-folded light curve does not approach zero suggests the absence of eclipsing events.

For reference, a schematic representation of the accretion pattern of AR UMa, as presented in Schmidt et al. (1999), is provided below:
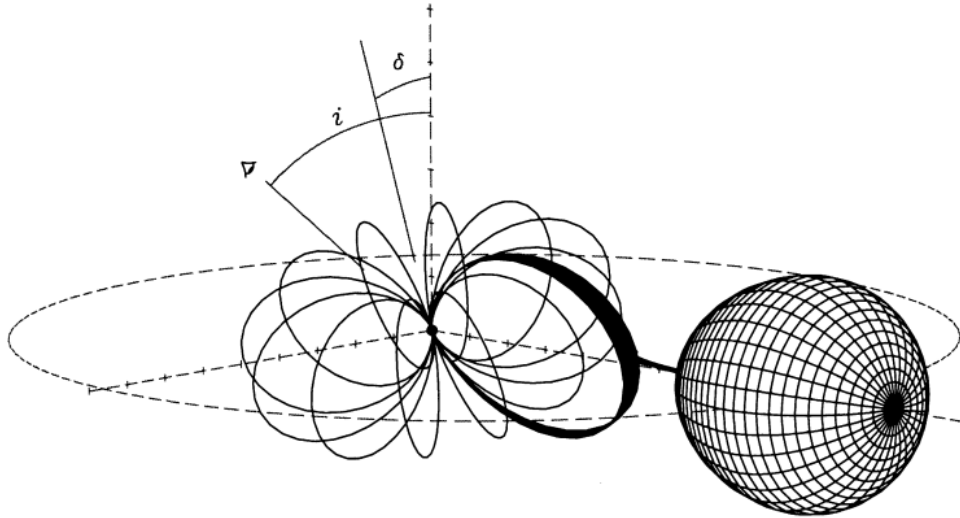
Figure 4.9: *Sketch of the AR UMa system with accretion active, using geometrical constraints derived (Source: Schmidt et al. (1999))*

4.5 Conclusions

Based on the above observations, we can draw the following conclusions about AR UMa:

- Observation State: AR UMa was observed by UVIT in a low state with a two-pole accretion mode.
- Orbital Period: The determined mean orbital period of the system is 1.932 hours.
- Absence of Eclipses: The absence of eclipses in the UVIT observations makes it challenging to deduce properties of the secondary component solely based on this data.

To gain further insights and confirm the identified properties, it is recommended to perform similar analyses in the optical and EUV spectra. Techniques such as plotting the periodogram and folding the light curves can be applied to verify the orbital period and accretion mode in these spectral ranges. The periodogram indicates the possibility of accretion disk precession due to the presence of a secondary dominant frequency (Fig 4.6) with a time period of 1.4 hours. However, additional investigations are required to conclusively determine whether this frequency is linked to precession or is merely noise. Analyzing data from different filters during the same observation period can provide valuable information in this regard.

Moreover, it is noteworthy that AR UMa lacks a high degree of optical polarization, which is a characteristic often observed in Polar AM Her Type systems (Schmidt et al. (1996)).

The properties of the system during the observation are presented below.

Observation date	May 22 2016
Epoch (JD)	2457530.757368444
Mean Flux (Filter F169M)	1.6689×10^{-14}
Mean Flux (Filter N263M)	5.1568×10^{-15}
Time Period	1.932 hours
Accretion State	Low
Accretion Mode	Double-pole

Table 4.5: Properties of AR UMa observed during UVIT observations

5. BL Hyi

5.1 Introduction

BL Hydri[1] is a polar cataclysmic variable located in the constellation Hydrus, close to the Small Magellanic Cloud. It was first discovered as part of the Warwick et al. (1981). Later in 1982, it was identified as an AM Her type star under the paper Visvanathan and Pickles (1982). BL Hyi is also referred to as "H 0139-68".
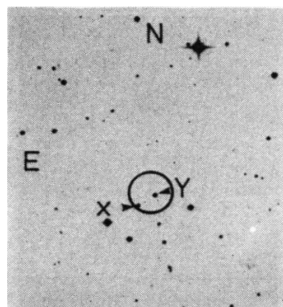

Figure 5.1: The circle of diameter 72 arcs defines the X-ray source location, and X marks the optical identification with H0139-68. (Source: A.J. Pickles)

Target	BL Hyi
Type	Polar
RA(α)	01h41m00.399s
Dec(δ)	-67d53m27.47s
Parallax(mas)	7.7163 ± 0.0513
Distance(pc)	~ 129
Period(hr)	1.9

Table 5.1: Properties of BL Hyi

---

[1]Studied by Ravi Kumar

5.2   Description

5.2.1   Flux

The table below shows the flux of BL Hyi varying with its orbital phase. The data was collected in the Ultra-Violet region using the International Ultraviolet Explorer (IUE) at 1550 and 1640Å.

C_{IV} (1550Å)	He_{II} (1640Å)	Orbital Phase
1.40e-12	3.27e-13	0.62
1.13e-13	1.36e-13	0.21
4.54e-13	1.04e-13	0.70
5.28e-13	1.18e-13	0.42
5.99e-13	1.32e-13	0.27
7.03e-13	1.84e-13	0.44
3.51e-12	9.24e-13	0.51
6.92e-13	2.31e-13	0.67

Table 5.2: Line Fluxes of C_{IV} and He_{II} in Units of (erg cm^{-2} s^{-1}) for BL Hyi
(Source: Sanad and Abdel-Sabour (2016))

5.2.2   Accretion

In optical studies, BL Hyi ranges from V band magnitude 14.9 to 16.4 during the high state and 16.9 to 17.5 during the low state.

The variation from low to high states reveals an increase in soft X-ray flares and a transition from one-pole to two-pole emission.

Date	Telescope/Observatory	Accretion State
1981 October	MSO	High
1983 November	CTIO	Low
1984 October	EXOSAT	Intermediate
1985 October	EXOSAT	Intermediate
1989 August	LCO and CTIO	Faint
1995 October	EUVE	High
1995 October	IUE	High
2003 June	HST	Low

Table 5.3: *Low, High and Intermediate States of BL Hyi*
(Sources: Araujo-Betancor et al. (2005), Szkody et al. (1997), Middleditch et al. (1997), Beuermann and Schwope (1989), Beuermann et al. (1985), Cowley et al. (1983), Visvanathan and Pickles (1982))

5.2.3   Astrosat Observations

The observations were taken by the UVIT under the observation ID G05_230T02_9000000548

Instrument	Filter ID	Start Time (UT)	End Time (UT)	Exposure (s)
UVIT FUV F1	F148W	2016-07-20 11:24:34	2016-07-20 17:02:36	20282.446
UVIT NUV F4	Grating	2016-07-20 11:24:34	2016-07-20 17:02:36	20282.446

Table 5.4: Details of the Astrosat Observation of BL Hyi

5.3 Image Processing and Analysis

5.3.1 Creating Master Images

After extracting and digesting L1 files into CCDLAB, our next step is to generate finalized master images that can be utilized for scientific analysis on the system. A thing to note is that the NUV images have Grating and are thus unusable for analysis.

(a) Raw NUV (Grating)   (b) Raw FUV Image   (c) Stacked FUV Image

Figure 5.2: Raw and Stacked images for FUV data of BL Hyi

We can see that no stacked image for NUV was produced due to the grating.

5.3.2 Final Science Images

Presentable images were made using DS9 which marks the system along with the coordinate system that was solved during image creation in CCDLAB.
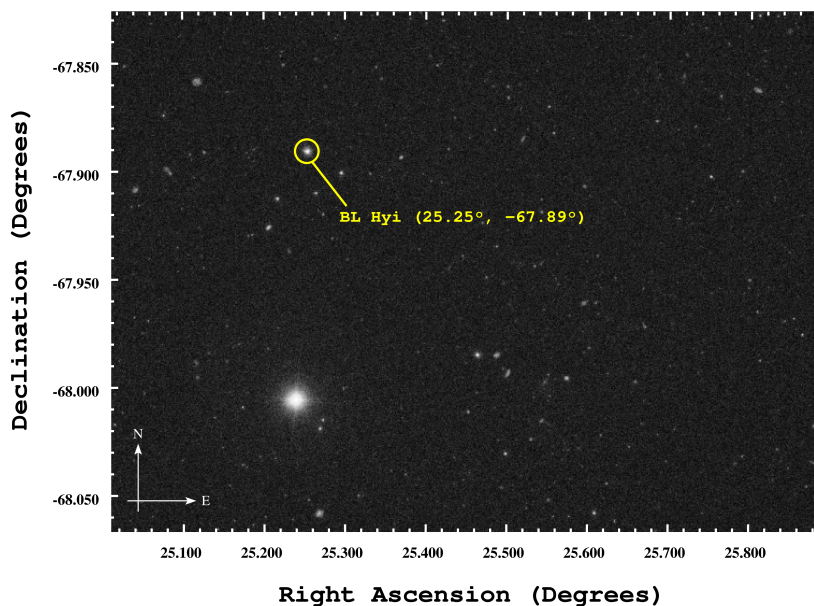

Figure 5.3: Final FUV Image

5.3.3 Surface Brightness Profile

A surface brightness plot provides an estimation of how brightness changes with respect to the radius. These plots are generated by creating Annuli regions on the system.
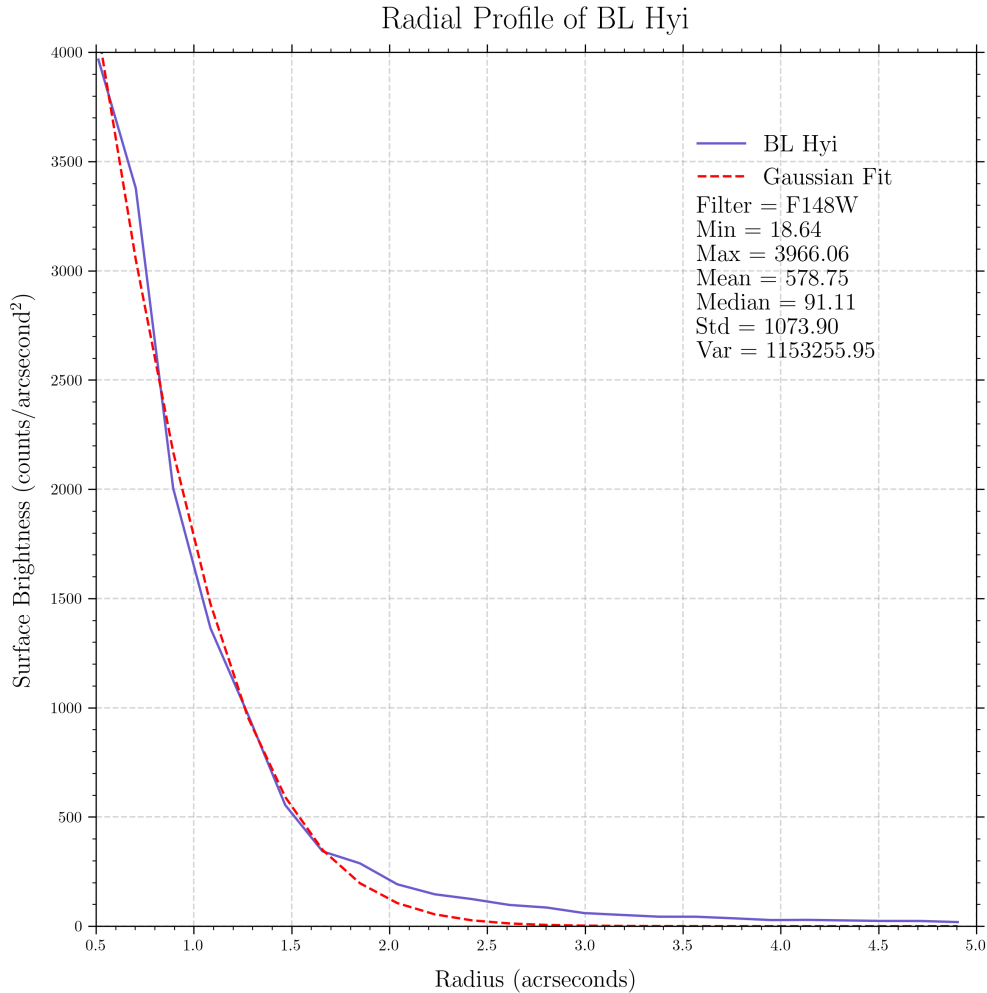

Figure 5.4: FUV Radial Profile

Based on the plots and the Gaussian fit to them, we can conclude that the source is a point source rather than an extended source.

5.4 Temporal Analysis

L2 data of BL Hyi was used to conduct timing analysis. Using Curvit on Python, the following light curves were plotted.
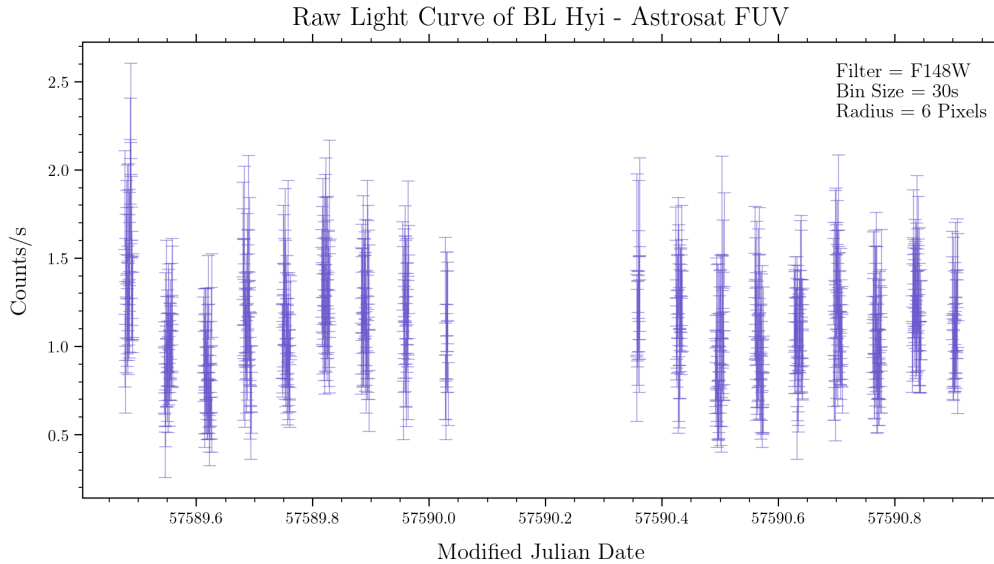

Figure 5.5: FUV light curve: Mean count rate = 1.117 cps

The mean count rates are 1.117 counts per second for the F148W filter. To convert the count rate into flux, the count rate is multiplied by the filter's unit conversion value (published on the ASTROSAT UVIT website).

Filter ID	Unit Conversion	Mean count rate (cps)	Flux (ergs cm^{-1} s^{-2} Å^{-1})
F148W	3.09×10^{-15}	1.117	3.42×10^{-15}

The mean wavelength of the FUV (F148W) filter is 1481Å with a $\Delta\lambda$ of 500 Å. This means that the CIV wavelength of 1550Å and HeII wavelength of 1640Å fall within this range and can be used to conclude the state of the system. Previous observations (Sanad and Abdel-Sabour, 2016) show that the system's high state luminosity in the CIV and HeII bands is 2×10^{31} ergs s^{-1} and 8×10^{30} ergs s^{-1} respectively. It has also been found that the intermediate state luminosity in the CIV and HeII bands is 3×10^{30} ergs s^{-1} and 6×10^{29} ergs s^{-1} respectively. This leads to the conclusion that the UVIT observations with an average luminosity of 3.4×10^{30} ergs s^{-1} recorded the system in its *intermediate state*.

Next, in order to find the period of the system, the Lomb-Scargle periodograms were plotted.
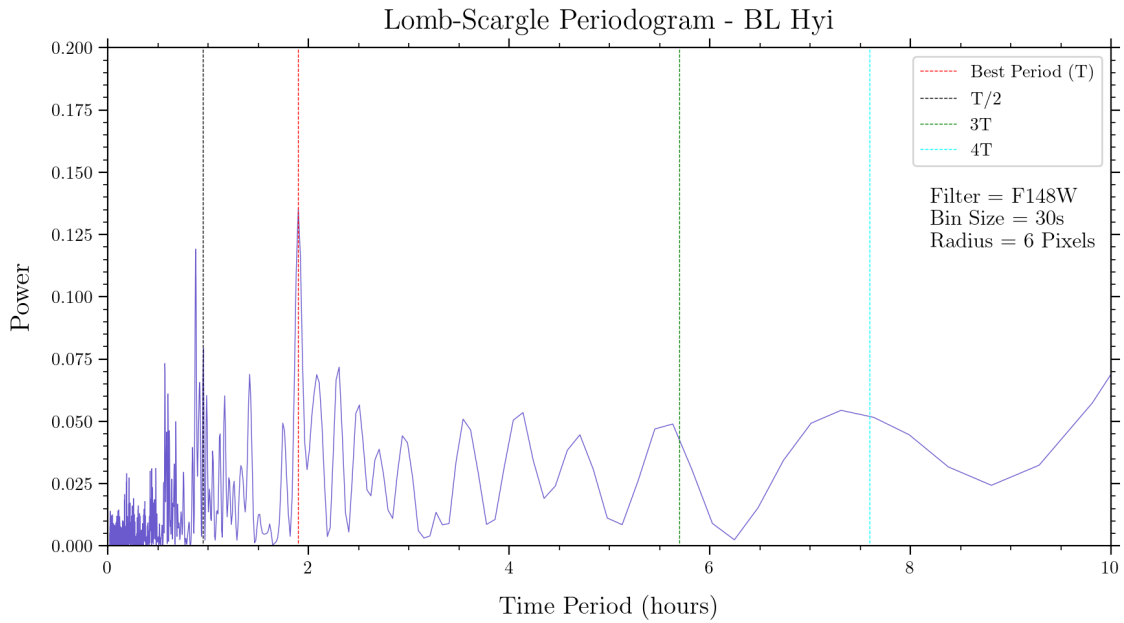

Figure 5.6: FUV periodogram: T = 1.897 hours

The time period of BL Hyi is found to be 1.897 hours, which is very close to the period values reported in Agrawal et al. (1983).

Now, the light curve can be folded to find out the accretion type. To do so, we use the Ephemeris of Cropper (1987) to correct for the phase of the system.

$$JD = 2444901.9744(9) + 0.07891507(18) \times E \tag{5.1}$$

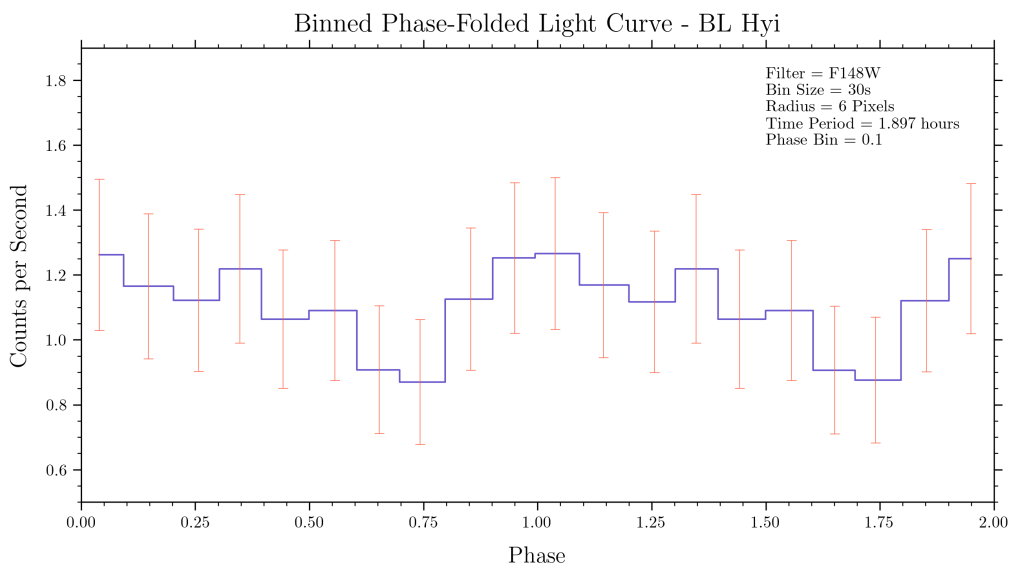The phase folded (folded using the period of 1.89 hours) light curve is shown below.

Figure 5.7: FUV Binned Phase Folded

The binned light curves seem to suggest a single-pole accretion mode as there seems to be only one peak in the entire light curve. As the light curve never goes near 0, there doesn't seem to be any eclipsing occurring from the secondary star blocking the view of the primary.

The following values and formulae obtained from the ASTROSAT UVIT website were used to convert the count rates into fluxes and magnitudes and plotted below.

Filter ID	Unit Conversion (UC)	Zero Point (ZP)
F148W	3.09×10^{-15}	18.016

Table 5.5: Table of values used to convert the count rate

The formulae used are:

$$\text{Flux } f_\lambda \text{ (in ergs cm}^{-2}\text{s}^{-1}\text{Å}^{-1}) = \text{Count Rate} \times \text{UC}$$

$$f = \Delta\lambda\, f_\lambda$$

$$\text{AB Magnitude} = -2.5\log_{10}(\text{Count Rate}) + \text{ZP}$$
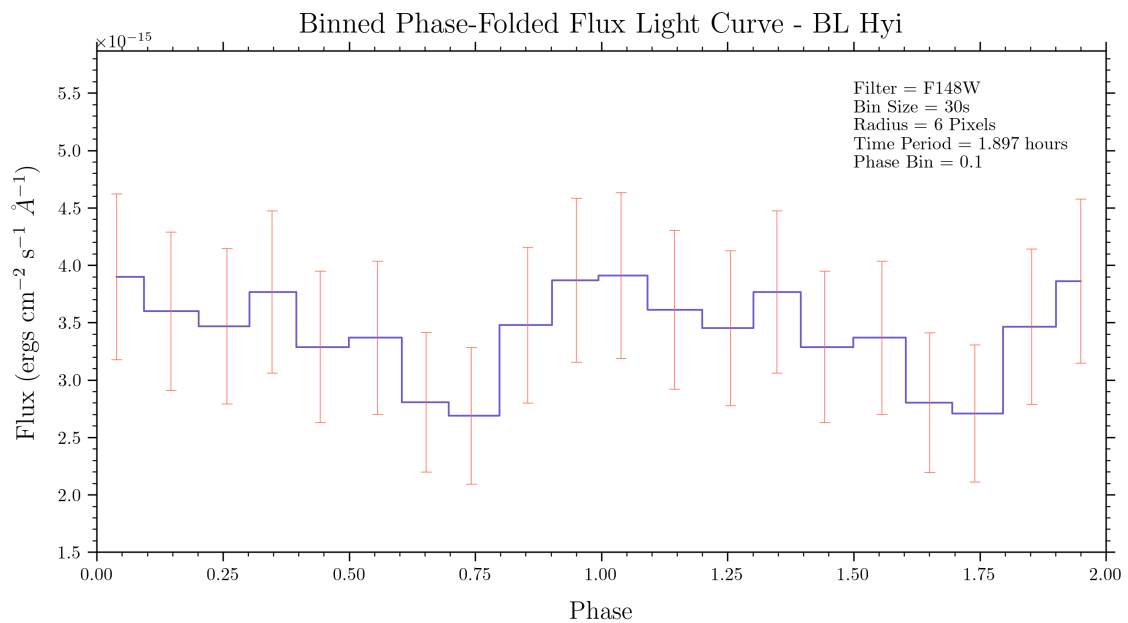

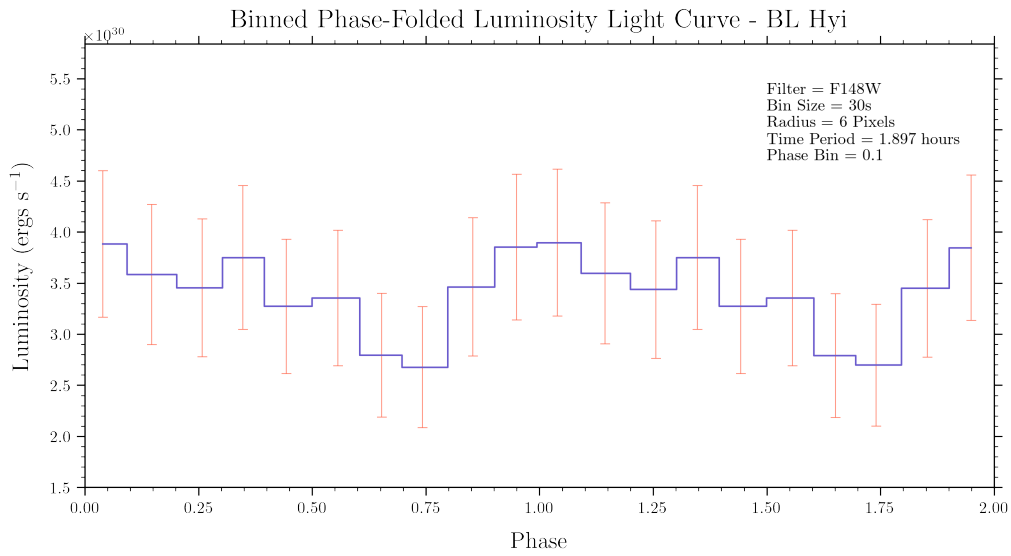Figure 5.8: Phase Folded Flux Light Curve
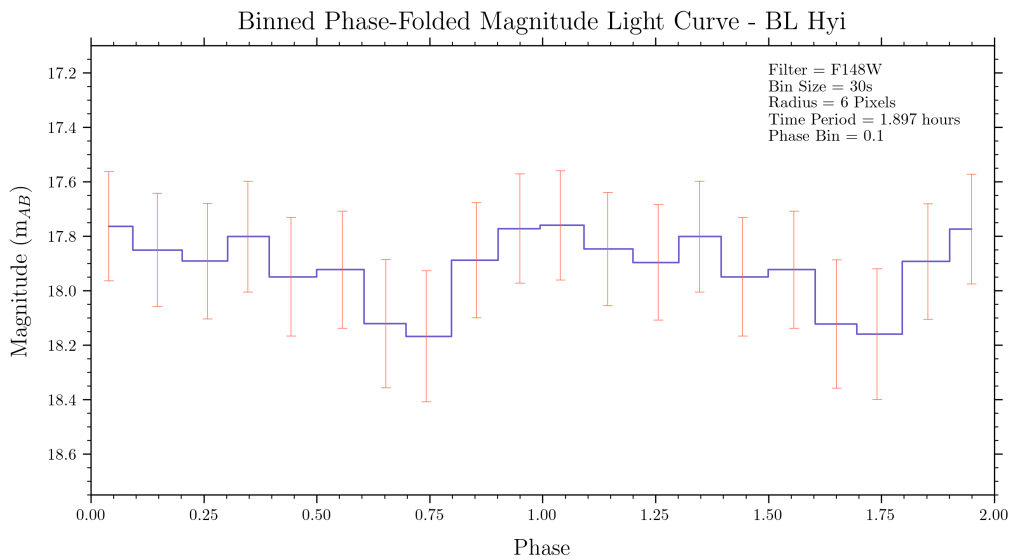
Figure 5.9: Phase Folded Luminosity Light Curve

Figure 5.10: Phase Folded Magnitude Light Curve

The properties of the system during the observation are presented below.

Observation date	August 20 2016
Epoch	2457589.9767581
Mean Flux (Filter F148W)	6.78
Time Period	1.897 hours
State	Intermediate
Accretion Mode	Single-pole

Table 5.6: Properties of BL Hyi observed during UVIT observations

6. QS Tel

6.1 Introduction

QS Telescopii[1] is a faint polar in the constellation Telescopium. It consists of a red dwarf orbiting around a white dwarf around 71% the mass of the Sun. The system was first discovered via the ROSAT WFC survey. The system is unique because its orbital period of 2.33 hours lies in the period gap of cataclysmic variables (Webbink and Wickramasinghe, 2002). The system is also known for frequently shifting between its high and low states and also for switching between single and double-pole accretion states (Traulsen, I. et al., 2011). The system is also referred to as "RE 1938-461".

Target	QS Tel
Type	Polar
RA(α)	$294.649208°$
Dec(δ)	$-46.215833°$
Parallax(mas)	5.3378 ± 0.0834
Distance(pc)	187 ± 3
Period(hr)	2.33

Table 6.1: Properties of QS Tel. Values from (Gaia Collaboration et al.)

---

[1] Studied by Shuban Ramesh Gupta

6.2 Description

6.2.1 Flux

The UVIT observations for QS Tel were made with the F154W (mean wavelength of 1541 Å) filter in the FUV region and the N245M (mean wavelength 2447 Å) filter in the NUV region. In order to study the variation of the properties of the system over time, past observations made in similar wavelength ranges are noted:

Observation Date	Instrument	State	Approx. Flux	Reference
August 1993	IUE CIV (1550)	high	200	de Martino et al. (1995)
June 1994	HST FOS CIV (1550)	high	200	de Martino et al. (1998)
June 1994	HST FOS (1420-1550)	high	260	de Martino et al. (1998)
June 1994	HST FOS (1900-2500)	high	600	de Martino et al. (1998)
September 1996	HST FOS CIV (1550)	low	20	Rosen et al. (2001)
September 1996	HST FOS (1900-2500)	low	210	Rosen et al. (2001)

Table 6.2: Observations of QS Tel in the UV region. Wavelengths are in units of Å and Flux in units of 10^{-14} ergs $cm^{-2}\ s^{-1}$

6.2.2 Accretion States

A table of the variation of the states of QS Tel over time is presented below:

Date of Observation	State	Reference
July-August 1992	low	Schwope et al. (1995)
September 1992	intermediate	Schwope et al. (1995)
August 1993	high	Schwope et al. (1995)
June 1994	high	de Martino et al. (1995)
April 1996	intermediate (single pole)	Rosen et al. (2001)
August 1996	deep low	Rosen et al. (2001)
August 2002	high	Romero-Colmenero et al. (2004)

Table 6.3: Variation of states of QS Tel

6.3   Image Processing

6.3.1   Creating Master Images

The details of the observations of QS Tel made by the UVIT are as follows:

Instrument	Filter ID	Start time (UT)	End time (UT)	Exposure (s)
Astrosat NUV F3	N245M	2017:08:04 10:33:36	2017:08:05 10:55:15	18763.367
Astrosat FUV F2	F154W	2017:08:04 10:33:40	2017:08:05 10:55:20	20130.743

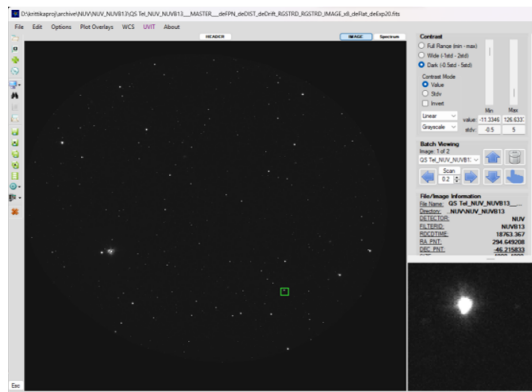Table 6.4: UVIT observation details

The images were produced using steps detailed in Section 2.2 and are displayed here
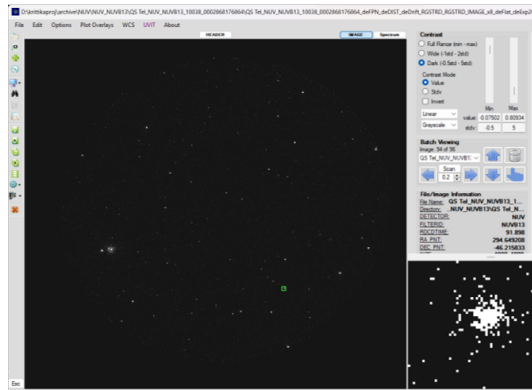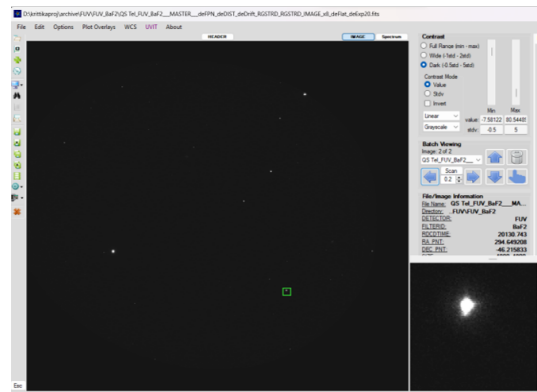

(a) Raw image from N245M Filter
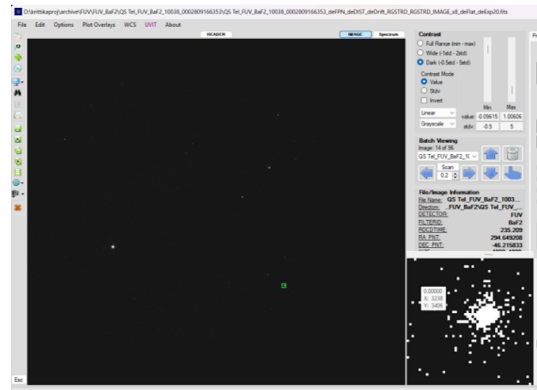
(b) Raw image from F154W Filter
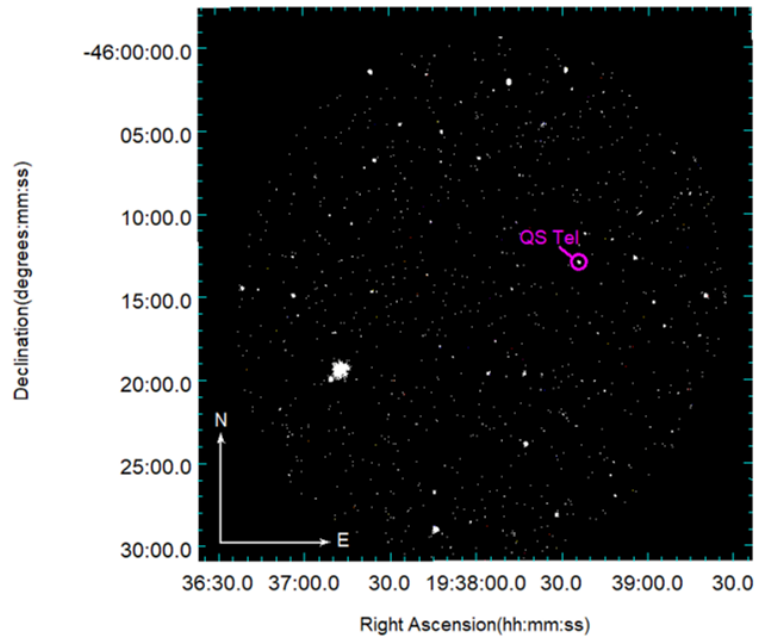

(c) Stacked image from N245M Filter

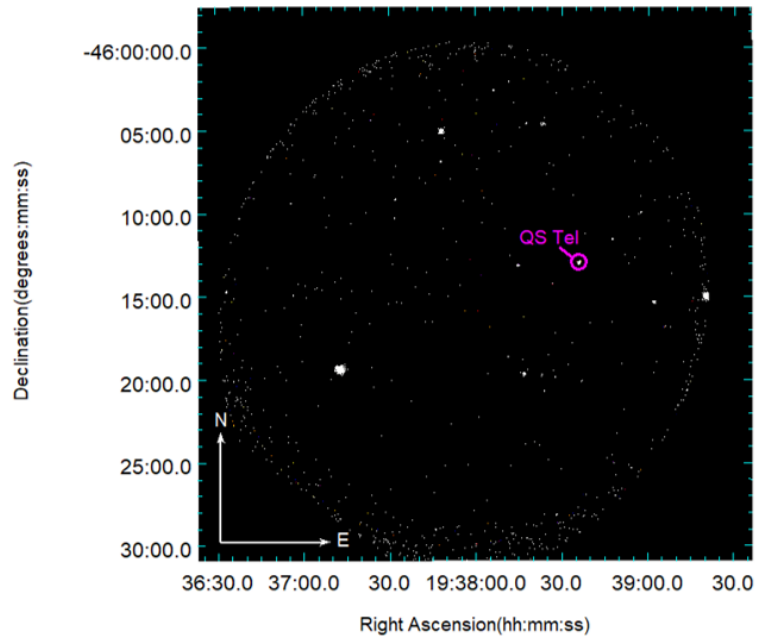(d) Stacked image from F154W Filter

Figure 6.1: Raw and Stacked images of QS Tel made using UVIT data

6.3.2 Final Science Images

The final exported science images are displayed below:
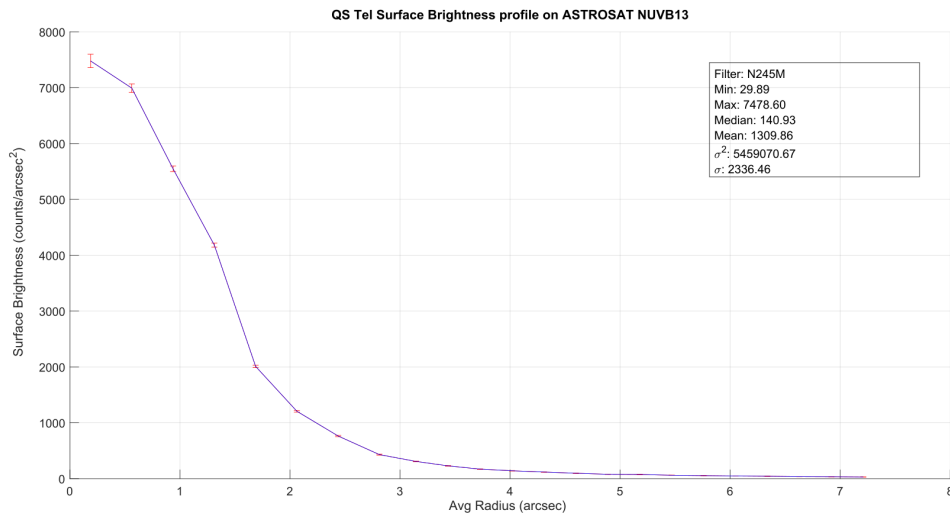

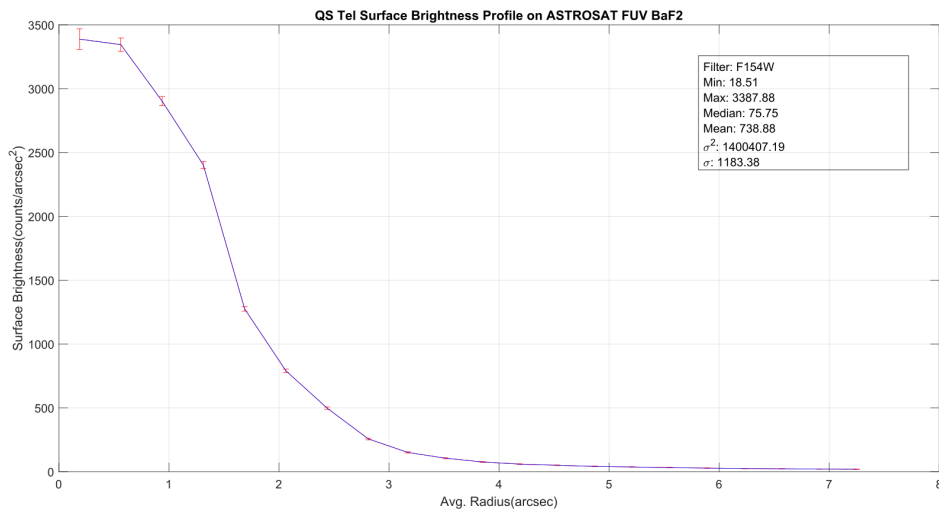(a) Final image from N245M Filter

(b) Final image from F154W Filter

Figure 6.2: Final science images

6.3.3 Surface Brightness Profiles

Additionally, the surface brightness profile was plotted for the system using DS9:
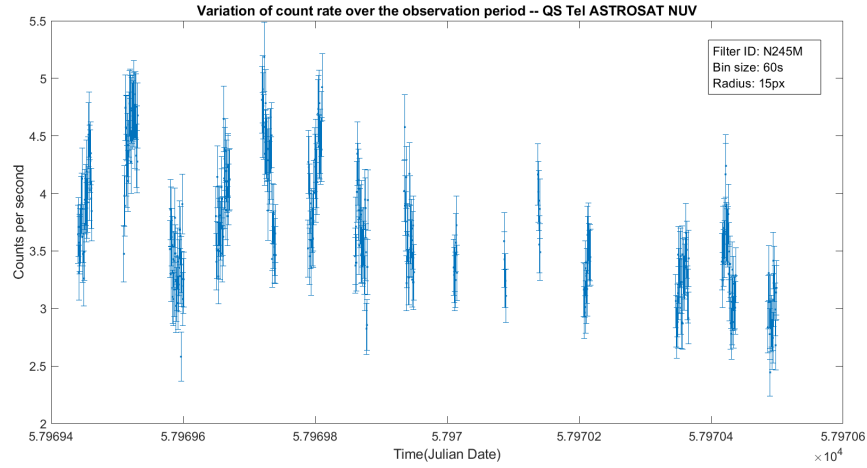

(a) NUV surface brightness profile
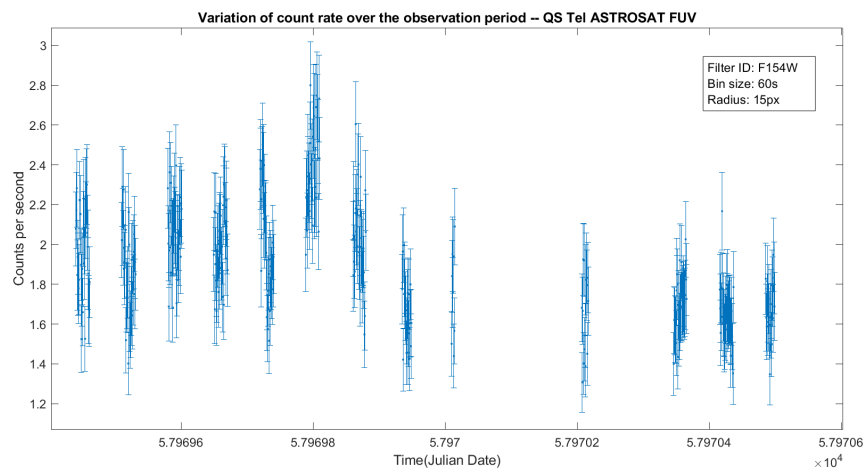

(b) FUV surface brightness profile

Figure 6.3: Surface brightness plots for QS Tel

6.4   Temporal Analysis

L2 data of QS Tel was used to conduct timing analysis. Using Curvit on Python, the following light curves were plotted.

(a) NUV light curve: Mean count rate = 3.71 cps

(b) FUV light curve: Mean count rate = 1.91 cps

Figure 6.4: Full light curves for QS Tel

The mean count rates are 3.71 and 1.91 counts per second for the N245M and F154W filters respectively. To convert the count rate into flux, the count rate is multiplied by the filter's unit conversion value (published on the ASTROSAT UVIT website).

Filter ID	Unit Conversion	Mean count rate (cps)	Flux (ergs cm^{-2} s^{-1} Å^{-1})
N245M	0.725×10^{-15}	3.71	2.69×10^{-15}
F154W	3.55×10^{-15}	1.91	6.78×10^{-15}

Table 6.5: Table of values used to convert count rates to flux

The mean wavelength of the FUV (F154W) filter is 1541Å with a $\Delta\lambda$ of 380 Å. This means that the CIV wavelength of 1550Å falls within this range and can be used to conclude the state of the system. Previous observations (Rosen et al., 2001) show that the system's low state flux in the CIV wavelength of 1550Å is 200×10^{-15} ergs cm^{-2} s^{-1}. This leads to an average flux of 6.78×10^{-15} ergs cm^{-2} s^{-1} Å^{-1} which multiplying by $\Delta\lambda$ gives 2576×10^{-15} ergs cm^{-2} s^{-1}. While this seems to suggest that the system was in high state, the values may be incorrect as continuum fluxes from our observation were compared to line fluxes from the paper. To counter this, the NUV observation with mean wavelength of 2447 Å can be compared to observations in the 1900-2500Å range. Here, the low state flux is 2100×10^{-15} ergs cm^{-2} s^{-1} (Rosen et al., 2001) while the observed flux is 2.69×10^{-15} ergs cm^{-2} s^{-1} Å^{-1} which multiplying by $\Delta\lambda$ of 280 Å gives 753×10^{-15} ergs cm^{-2} s^{-1} which is lower than the observed low state flux and is on the same order of magnitude. This lets us conclude that QS Tel is indeed in low state in the UVIT observations.

Next, in order to find the period of the system, the Lomb-Scargle periodograms were plotted.
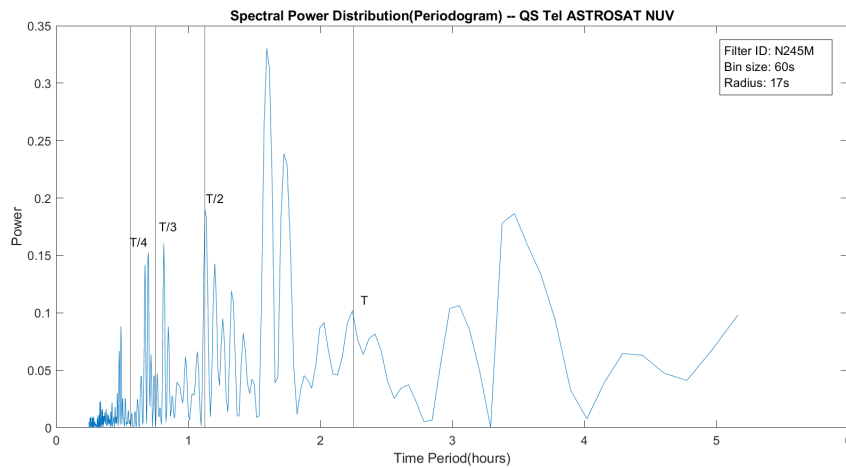

(a) NUV periodogram: T=2.244 hours
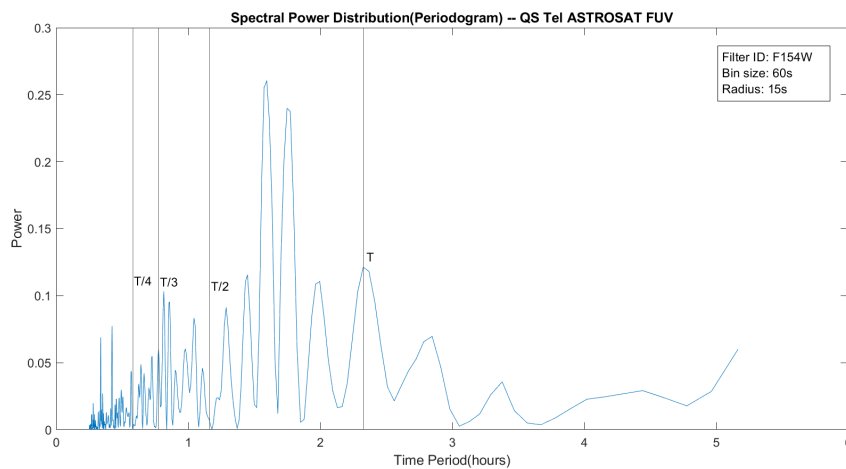

(b) FUV periodogram: T=2.326 hours

Figure 6.5: Power spectral density plots for QS Tel

As QS Tel is a relatively faint source in its low state, noise from various sources becomes significant and makes its way into the data. This effect is very evident in the power spectral density plots where the period with the highest power (around 1.6 hours) is not even close to the actual period of the system, and the peak around the actual period has a lower yet significant power. As both the periodograms give a slightly different time period around the peak of the actual time period, the two time periods are averaged to obtain the time period of the system in the observation. This time period is 2.285 hours and lies in the period gap of CVs.

Now, the light curve can be folded to find out the accretion type. To do so, the epoch was obtained from Schwope et al. (1995) as Julian Date 2448894.5417 The phase folded light curves using the time period of 2.285 hours. The phase folded light curves are presented below.
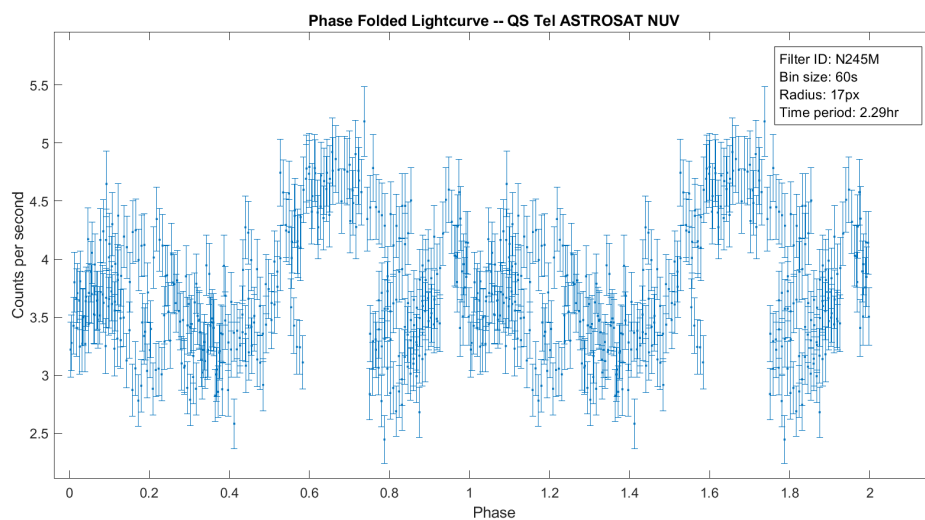
(a) NUV phase folded light curve
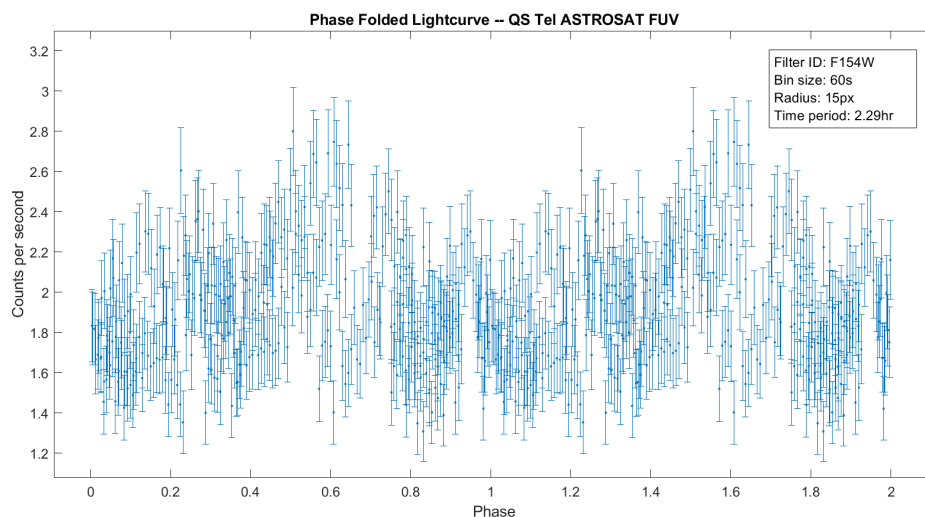
(b) FUV phase folded light curve

Figure 6.6: Phase folded light curves for QS Tel

The phase folded curve is very cluttered and needs to be binned to make the

variation clearer. To do so, the data was binned into phases of 0.05 and plotted.

The binned light curves are presented below after converting count rates to flux:
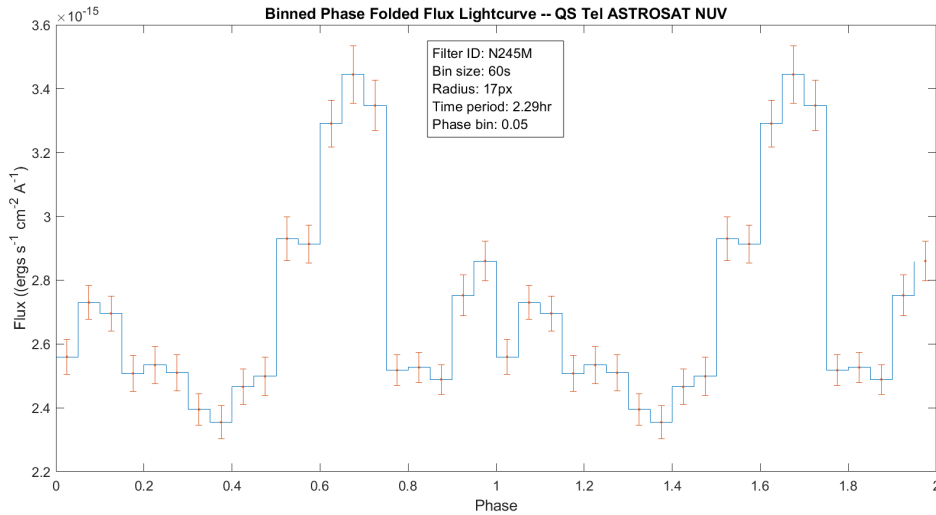
(a) NUV binned light curve
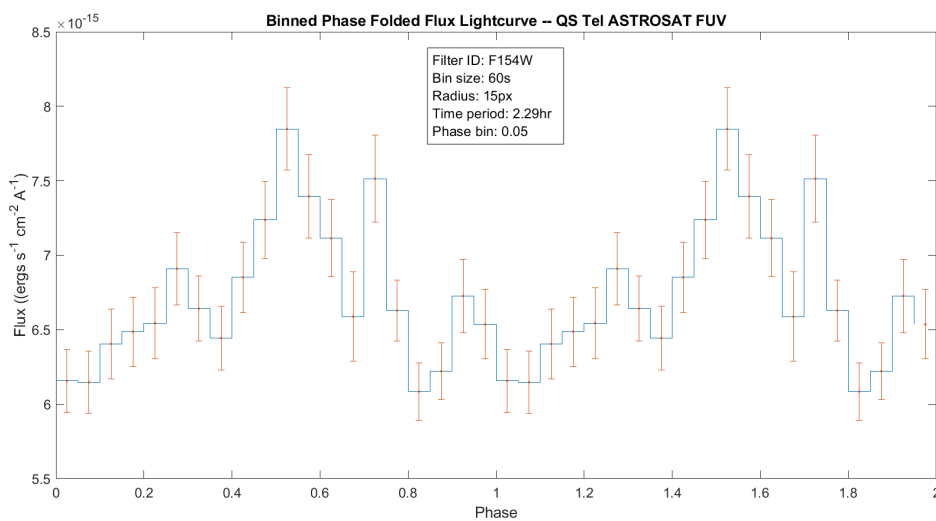
(b) FUV binned light curve

Figure 6.7: Binned light curves for QS Tel

The binned light curves seem to suggest a two-pole accretion mode as there seem to be two peaks (one at phase ≈ 0.6 and one at phase ≈ 1). As the light curve never goes near 0, there doesn't seem to be any eclipsing occurring from the secondary star blocking the view of the primary.

The following values and formulae obtained from the ASTROSAT UVIT website were used to convert the count rates into fluxes and magnitudes and plotted below.

Filter ID	Unit Conversion (UC)	Zero Point (ZP)
N245M	0.725×10^{-15}	18.50
F154W	3.55×10^{-15}	17.778

Table 6.6: Table of values used to convert the count rate

The formulae used are:

$$\text{Flux (in ergs cm}^{-2}\text{ s}^{-1}\text{ Å}^{-1}) = \text{Count Rate} \times \text{UC}$$

$$\text{AB Magnitude} = -2.5\log_{10}(\text{Count Rate}) + \text{ZP}$$

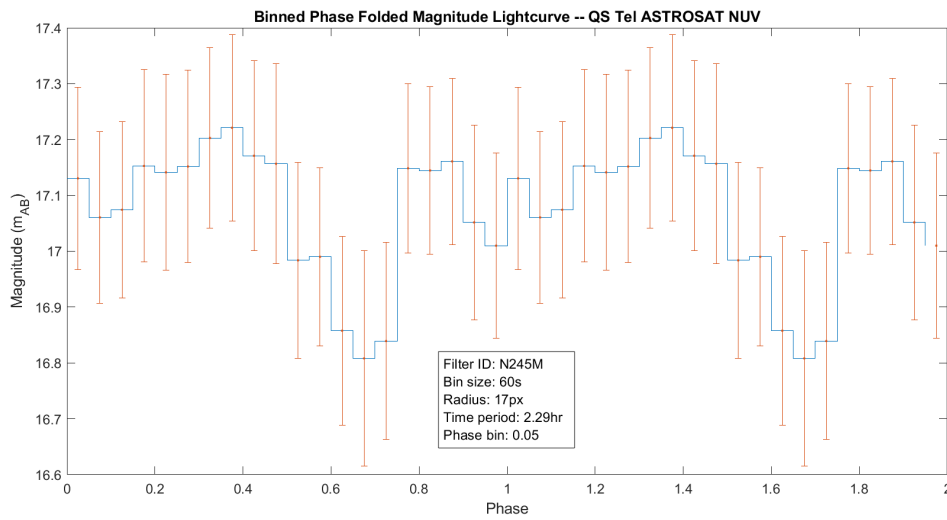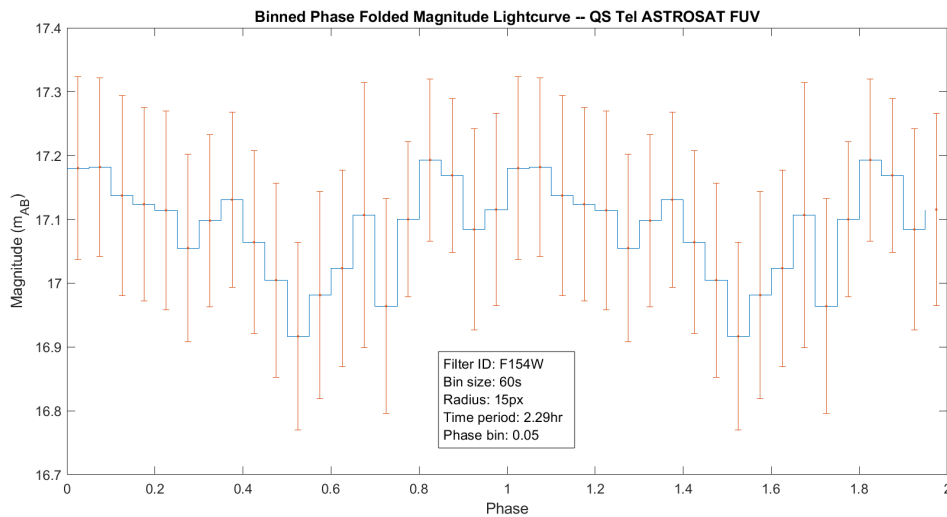The variation of magnitudes over time is presented below:

(a) NUV Magnitude vs Phase

(b) FUV Magnitude vs Phase

Figure 6.8: Binned magnitude light curves for QS Tel

6.5 Conclusions

From the above observations, it can be concluded that UVIT observed the system in a low state with a two-pole accretion mode. As the observations showed no eclipses, it would be difficult to ascertain properties of the secondary from the UVIT observations alone. The system has an average AB magnitude of 17.075 and a mean period of 2.285 hours. To confirm the above properties, SXT (Soft X-ray Telescope) data from ASTROSAT can be used. If the system is in its low state, a soft x ray flux of about 0.025 counts per second is expected as observed by Rosen et al. (2001). Similar analyses like plotting the periodogram and folding the light curves can be used to confirm the orbital period and accretion mode. The periodogram seems to suggest accretion disk precession due to a dominant frequency with time period of 1.6 hours, but further analysis is required to truly ascertain whether this is due to precession or noise. This can again be performed by analyzing data from different filters during the same observation period. As the system is in low state, a circular polarization of around 10 percent can be expected in the 3400-5700 bands (Ferrario et al., 1994).

A summary of properties is provided below.

Observation date	August 4 & 5 2017
Epoch	2448894.5417
Mean Flux (Filter N245M)	2.69
Mean Flux (Filter F154W)	6.78
AB Magnitude (Filter N245M)	17.07
AB Magnitude (Filter N245M)	17.08
Mean Period	2.285 hours
State	Low
Accretion Mode	Two-pole

Table 6.7: Summary of properties of QS Tel observed during UVIT observations. Fluxes are in units of $\times 10^{-15}$ ergs cm^{-2} s^{-1} Å^{-1}

7. Conclusion

In this project, we conducted extensive observations of 3 AM Her Type MCVs using UVIT (Ultraviolet Imaging Telescope) and analyzed the acquired data to gain insights into the system's behavior and characteristics. To further validate and expand our findings, we can perform similar analyses in the Soft X-ray, optical, and EUV spectra, involving techniques such as plotting the periodogram and folding the light curves. Such investigations can help verify the orbital period and accretion mode, with the periodogram suggesting the possibility of accretion disk precession. Additionally, we carried out astrometry and image processing in the project. Astrometry is crucial in astrophysics as it involves measuring the precise positions of celestial objects. Image processing, on the other hand, enables us to enhance and analyze the acquired images, extracting valuable information about the target object's properties and morphology.

In the future, we can also explore the long-term variability of AR UMa, specifically looking for any secular trends in the orbital or pulsation periods. Long-term variability refers to changes in the observed properties of a celestial object over extended periods, ranging from months to years or even longer. Incorporating spectral analysis on the data from UVIT would be a valuable enhancement to our study.

Overall, combining spectral analysis with the other observational techniques mentioned earlier can lead to a more comprehensive understanding of MCVs and their accretion behavior. It can also provide a basis for comparison with theoretical models and contribute to the broader knowledge of cataclysmic variable stars and their evolution.

We would like to express our gratitude to IIT Bombay, the Krittika Astronomy Club, and our mentor Abhinna Sundar for their support and resources throughout this project. Their contribution has been instrumental in the successful execution of this research endeavor.

Bibliography

S. N. Tandon, Annapurni Subramaniam, V. Girish, J. Postma, K. Sankarasubramanian, S. Sriram, C. S. Stalin, C. Mondal, S. Sahu, P. Joseph, J. Hutchings, S. K. Ghosh, I. V. Barve, K. George, P. U. Kamath, S. Kathiravan, A. Kumar, J. P. Lancelot, D. Leahy, P. K. Mahesh, R. Mohan, S. Nagabhushana, A. K. Pati, N. Kameswara Rao, Y. H. Sreedhar, and P. Sreekumar. In-orbit Calibrations of the Ultraviolet Imaging Telescope. AJ, 154(3):128, September 2017. doi: 10.3847/1538-3881/aa8451.

S. N. Tandon, J. Postma, P. Joseph, A. Devaraj, A. Subramaniam, I. V. Barve, K. George, S. K. Ghosh, V. Girish, J. B. Hutchings, P. U. Kamath, S. Kathiravan, A. Kumar, J. P. Lancelot, D. Leahy, P. K. Mahesh, R. Mohan, S. Nagabhushana, A. K. Pati, N. Kameswara Rao, K. Sankarasubramanian, S. Sriram, and C. S. Stalin. Additional Calibration of the Ultraviolet Imaging Telescope on Board AstroSat. AJ, 159(4):158, April 2020. doi: 10.3847/1538-3881/ab72a3.

Joseph E. Postma and Denis Leahy. UVIT data reduction pipeline: A CCDLAB and UVIT tutorial. *Journal of Astrophysics and Astronomy*, 42(2):30, October 2021. doi: 10.1007/s12036-020-09689-w.

Smithsonian Astrophysical Observatory. SAOImage DS9: A utility for displaying astronomical images in the X11 window environment. Astrophysics Source Code Library, record ascl:0003.002, March 2000.

Jacob T. VanderPlas. Understanding the Lomb-Scargle Periodogram. ApJS, 236(1): 16, May 2018. doi: 10.3847/1538-4365/aab766.

J. A. Mattei and J. R. Percy. Hands-On Astrophysics: Variable Stars in Math, Science, and Computer Education. In *American Astronomical Society Meeting Abstracts*, volume 195 of *American Astronomical Society Meeting Abstracts*, page 106.08, December 1999.

R. A. Remillard, J. F. Schachter, A. D. Silber, and P. Slane. 1ES 1113+432: Luminous, Soft X-Ray Outburst from a Nearby Cataclysmic Variable (AR Ursae Majoris). ApJ, 426:288, May 1994. doi: 10.1086/174063.

Gary D. Schmidt, Paula Szkody, Paul S. Smith, Andrew Silber, Gaghik Tovmassian, D. W. Hoard, B. T. Gänsicke, and D. De Martino. Ar ursae majoris: The first high-field magnetic cataclysmic variable. *Astrophysical Journal*, 473(1 PART I):483–493, 1996. ISSN 0004-637X. doi: https://doi.org/10.1086/178160.

Paula Szkody, Stéphane Vennes, Gary D. Schmidt, R. Mark Wagner, Robert Fried, Allen W. Shafter, and Erik Fierce. Asca, rxte, euve, and optical observations of the high magnetic field cataclysmic variable ar ursae majoris. *The Astrophysical Journal*, 520(2):841, aug 1999. doi: 10.1086/307505. URL https://dx.doi.org/10.1086/307505.

Gary D. Schmidt, D. W. Hoard, Paula Szkody, Fulvio Melia, R. Kent Honeycutt, and R. M. Wagner. Accretion in the high-field magnetic cataclysmic variable ar ursae majoris*. *The Astrophysical Journal*, 525(1):407, nov 1999. doi: 10.1086/307901. URL https://dx.doi.org/10.1086/307901.

D. W. Hoard, Gary D. Schmidt, Paula Szkody, Lilia Ferrario, Oliver Fraser, Michael A. Wolfe, and B. T. Gänsicke. The ultraviolet spectrum of the high-field magnetic cataclysmic variable ar ursae majoris*. *The Astronomical Journal*, 128(4):1894, oct 2004. doi: 10.1086/423918. URL https://dx.doi.org/10.1086/423918.

R. S. Warwick, N. Marshall, G. W. Fraser, M. G. Watson, A. Lawrence, C. G. Page, K. A. Pounds, M. J. Ricketts, M. R. Sims, and A. Smith. The Ariel V (3A) catalogue of X-ray sources. I. MNRAS, 197:865–891, December 1981. doi: 10.1093/mnras/197.4.865.

N. Visvanathan and A. Pickles. Optical identification of X-ray source H0139 - 68 with an AM Herculis-type system. Nature, 298(5869):41–44, July 1982. doi: 10.1038/298041a0.

M. R. Sanad and M. A. Abdel-Sabour. Ultraviolet Spectroscopy of BL Hyi and EF Eri in High and Intermediate States. AJ, 152(2):37, August 2016. doi: 10.3847/0004-6256/152/2/37.

Sofia Araujo-Betancor, Boris T. Gänsicke, Knox S. Long, Klaus Beuermann, Domitilla de Martino, Edward M. Sion, and Paula Szkody. Far-Ultraviolet Spectroscopy of Magnetic Cataclysmic Variables. ApJ, 622(1):589–601, March 2005. doi: 10.1086/427914.

Paula Szkody, Stéphane Vennes, Edward M. Sion, Knox S. Long, and Steve B. Howell. Extreme Ultraviolet Photometry and Spectroscopy of BL Hydri. ApJ, 487(2):916–920, October 1997. doi: 10.1086/304660.

John Middleditch, James N. Imamura, and Thomas Y. Steiman-Cameron. Discovery of Quasi-periodic Oscillations in the AM Herculis Object BL Hydri. ApJ, 489(2):912–916, November 1997. doi: 10.1086/304834.

K. Beuermann and A. D. Schwope. One-pole and two-pole X-ray emission in the AM Herculis binary BL Hyi. A&A, 223:179–186, October 1989.

K. Beuermann, A. Schwope, H. Weissieker, and C. Motch. EXOSAT / Optical Observations of the Am-Herculis Star H0139-68. Space Sci. Rev., 40(1-2):135–138, February 1985. doi: 10.1007/BF00212876.

A. Cowley, J. Hutchings, and D. Crampton. 0139-68. IAU Circ., 3895:2, November 1983.

P. C. Agrawal, G. R. Riegler, and A. R. Rao. A new AM Her-like X-ray source. Nature, 301(5898):318–321, January 1983. doi: 10.1038/301318a0.

Mark Cropper. Polarimetry of BL HYI (H 0139-68) in high and low states. MNRAS, 228:389–399, September 1987. doi: 10.1093/mnras/228.2.389.

R. F. Webbink and D. T. Wickramasinghe. Cataclysmic variable evolution: AM Her binaries and the period gap. MNRAS, 335(1):1–9, September 2002. doi: 10.1046/j.1365-8711.2002.05495.x.

Traulsen, I., Reinsch, K., Schwope, A. D., Burwitz, V., Dreizler, S., Schwarz, R., and Walter, F. M. Xmm-newton observations of the x-ray soft polar qs telescopii. *A&A*, 529:A116, 2011. doi: 10.1051/0004-6361/201016352. URL https://doi.org/10.1051/0004-6361/201016352.

Gaia Collaboration, A. G. A. Brown, A. Vallenari, T. Prusti, and journal = A&A keywords = catalogs, astrometry, techniques: radial velocities, stars: fundamental parameters, stars: variables: general, minor planets, asteroids: general, Astrophysics - Astrophysics of Galaxies, Astrophysics - Instrumentation and Methods for Astrophysics year = 2018 month = aug volume = 616 eid = A1 pages = A1 doi = 10.1051/0004-6361/201833051 archivePrefix = arXiv eprint = 1804.09365 primaryClass = astro-ph.GA adsurl = https://ui.adsabs.harvard.edu/abs/2018AA...616A...1G adsnote = Provided by the SAO/NASA Astrophysics Data System de Bruijne, title = "Gaia Data Release 2. Summary of the contents and survey properties".

D. de Martino, D. A. H. Buckely, M. Mouchet, and K. Mukai. UV observations of the polar system RE 1938-461. A&A, 298:L5, June 1995.

D. de Martino, M. Mouchet, S. R. Rosen, B. T. Gänsicke, K. L. Clayton, and K. O. Mason. Insights into the accretion flow in QS Telescopii (RE1938-461) from HST observations. A&A, 329:571–578, January 1998.

S. R. Rosen, J. F. Rainger, M. R. Burleigh, J. P. D. Mittaz, D. A. H. Buckley, M. M. Sirk, R. Lieu, S. B. Howell, and D. de Martino. Multiwavelength monitoring of QS Tel. *Monthly Notices of the Royal Astronomical Society*, 322(3):631–642, 04 2001. ISSN 0035-8711. doi: 10.1046/j.1365-8711.2001.04141.x. URL https://doi.org/10.1046/j.1365-8711.2001.04141.x.

A. D. Schwope, H. C. Thomas, K. Beuermann, V. Burwitz, S. Jordan, and R. Haefner. Two-pole accretion in the high-field polar RXJ 1938.6-4612. A&A, 293:764–776, January 1995.

E. Romero-Colmenero, S. B. Potter, and D. A. H. Buckley. Spectroscopic and polarimetric observations of qs tel. *Astronomische Nachrichten*, 325(3):214–214, 2004. doi: https://doi.org/10.1002/asna.200310216. URL https://onlinelibrary.wiley.com/doi/abs/10.1002/asna.200310216.

Lilia Ferrario, Dayal. T. Wickramasinghe, Jeremy A. Bailey, David A. H. Buckley, and
Jim H. Hough. The polarization and magnetic field of RE J1938 − 461 during its
low state. *Monthly Notices of the Royal Astronomical Society*, 268(1):128–134, 05
1994. ISSN 0035-8711. doi: 10.1093/mnras/268.1.128. URL https://doi.org/10.1093/
mnras/268.1.128.